2017-01-01

Development and Verification of a Lab-Scale Green Propellant Hybrid Motor System

Shyamal Patel
University of Texas at El Paso, shyamal42892@gmail.com

DEVELOPMENT AND VERIFICATION OF A LAB-SCALE GREEN PROPELLANT HYBRID MOTOR SYSTEM

SHYAMAL PATEL

Master's Program in Mechanical Engineering

APPROVED:

Norman Love, Ph.D., Chair

Ahsan R. Choudhuri, Ph.D.

Tzu-Liang Tseng, Ph.D.

Charles Ambler, Ph.D.
Dean of the Graduate School

Dedication

I would like to dedicate this work to the friends, family, and mentors who have helped me throughout my education.

DEVELOPMENT AND VERIFICATION OF A LAB-SCALE GREEN PROPELLANT HYBRID MOTOR SYSTEM

by

SHYAMAL JANAK PATEL, B.S. Aerospace Engineering

THESIS

Presented to the Faculty of the Graduate School of

The University of Texas at El Paso

in Partial Fulfillment

of the Requirements

for the Degree of

MASTER OF SCIENCE

Department of Mechanical Engineering

THE UNIVERSITY OF TEXAS AT EL PASO

May 2017

Acknowledgements

I would like to thank the Missile Defense Agency for the financial support that allowed me to conduct research and complete my thesis. The material in this project is based upon the work supported by MDA under award HQ0147-15-C-6001 and any opinions, findings, conclusions, or recommendations expressed herein are those of the authors and do not necessarily reflect the views of the agency. I would also like to express my gratitude to my advisor Dr. Norman Love and Dr. Ahsan Choudhuri for this amazing opportunity and for their support and wisdom throughout my years at UTEP. I would also like to express gratitude to Charles Hill for his technical guidance, a significant contribution to my research efforts. A special thanks goes to my parents, friends and family for their support and encouragement.

Table of Contents

Acknowledgements v

Table of Contents vi

List of Tables viii

List of Figures ix

Chapter 1: Introduction and Background 1

1.1 Liquid Bi-Propellant Propulsion Systems 1

1.2 Solid Propulsion Systems 2

1.3 Hybrid Propulsion Systems 3

1.4 Hydroxyl Ammonium Nitrate 5

1.5 Project Overview 7

1.6 Project Relevance 7

Chapter 2: Background 9

2.1 Regression Rate 9

2.1 HAN Decomposition 12

Chapter 3: Experimental Design 16

3.1 Test Setup 16

3.1.1 Delivery and Purge System 19

3.1.2 HTPB Fuel Grain 23

3.1.3 Fuel Grain Holder 26

3.1.4 Methane Ignition System 29

3.1.5 Exhaust System 30

3.2 GOx and HTPB Methodology 31

3.3 HAN and HTPB Experiments 32

Chapter 4: Results and Analysis 34

4.1 GOx/HTPB Hot-Fire Results 34

4.1.1 Regression Rate 34

4.1.2 Specific Impulse 39

4.2 Regression Rate of HAN/HTPB 40

4.2.1 Regression Rate 40

4.2.1 Specific Impulse 43

Chapter 5: Conclusion....47

5.1 Summary 47

5.2 Future Work 48

References....49

Appendix A: HAN Decomposition CEA Analysis....51

Appendix B: Burner Support Drawing 54

Appendix C: HTPB Mixing Procedure....55

Appendix D: GOx and HTPB Flame Lengths 65

Appendix E: Specific Impulse Sample Calculations 66

Appendix F: Regression Rate Sample Calculations 67

Appendix G: Uncertainty Sample Calculations....68

Vita 69

List of Tables

Table 1.1: Performance of hybrid propellant, Pc = 500 psia and Pe = 14.7 psia [1] 4
Table 1.2: Properties of commonly used monopropellants [3,17] 5
Table 1.3: Performance comparison for various oxidizers with HTPB, PE, and DCPD, *P* = 1000 psi, sea-level expansion. [8] 6
Table 2.1: HAN decomposition products from CEA 15
Table 3.1: HTPB and Oxygen Hot-Fire Test Matrix 32
Table 3.2: HAN Decomposition and HTPB Hot-Fire Test Matrix 33
Table E.1: Parameters for Liquid Oxygen and HTPB hybrid motor 66

List of Figures

Figure 1.1: Schematic of a liquid bi-propellant rocket system [4] 2
Figure 1.2: Schematic of solid propellant rocket system [4] 3
Figure 2.1: Illustration of the internal ballistics of hybrid motors [15]. 9
Figure 2.2: Illustration of the boundary layer developed in a hybrid motor [15]. 10
Figure 2.3: Thermal decomposition of 40% HAN solution [5,6] 13
Figure 2.4: Catalytic decomposition of 40% HAN solution [5,6] 13
Figure 2.5: Evolution of species concentrations during thermal decomposition of 13 M HAN solution at 180°C [11]. 14
Figure 3.1: Gaseous oxygen and HTPB schematic 17
Figure 3.2: Small-scale GOx and HTPB test setup 17
Figure 3.3: HAN decomposition gases and HTPB test rig schematic. 18
Figure 3.4: Fully integrated HAN decomposition and HTPB test rig. 19
Figure 3.5: Delivery system for (a) gaseous oxygen and (b) HAN decomposition test setup. 20
Figure 3.6: Normally closed isolation valve used for oxygen. 21
Figure 3.7: Omega FMA 1700A/1800A series mass flowmeters used to monitor flowrates. 21
Figure 3.8: New Era syringe pump used to inject water into heated coil. 22
Figure 3.9: Heated coils used to evaporate water to generate steam. 23
Figure 3.10: Dimensions of the HTPB fuel grains. 25
Figure 3.11: Fully cured and perforated HTPB fuel grain. 25
Figure 3.12: Fuel grain holder dimensions. 27
Figure 3.13: Fuel grain holder assembly and installation. 28
Figure 3.14: Fuel grain holder assembly illustrating thermocouple placements 29
Figure 3.15: Handheld igniter 29
Figure 3.16: Igniter assembly 30
Figure 3.17: Exhaust dome used to capture exhaust products during testing. 31
Figure 4.1: Experimental regression rate obtained for mass flux of 0.25 – 0.63 g/cm^2-s. 35
Figure 4.2: Motor 8 inlet after (a) the initial 10 second burn and (b) secondary 20 second burn. 36
Figure 4.3: Motor 6 outlet for (a) initial 10 second burn and (b) secondary 20 second burn. 38
Figure 4.4: Motor 6 port after 20 second burn 39
Figure 4.5: Specific impulse estimates for the oxygen and HTPB hot-fire tests. 40
Figure 4.6: (a) The methane diffusion flame followed by (b, c) an ignition between the oxidizers and methane ending with (d) an extinguished motor. 41
Figure 4.7: Surface of the fuel grain inlet displaying the condensed water gathered from testing. 42
Figure 4.8: Adiabatic flame temperature for the methane and oxygen pilot flame with increasing nitrogen concentration ranged over an increasing steam concentration. 43
Figure 4.9: CEA predictions of specific impulse for AF-M315E, Pc = 25 psia. 44
Figure 4.10: CEA predictions of specific impulse for AFM-315E decomposition gases, Pc = 25 psia. 45
Figure 4.11: CEA predictions of specific impulse for HAN decomposition gases, Pc = 25 psia. 46
Figure C.1: Average flame length observed for each motor. 65

Chapter 1: Introduction

Hybrid rockets demonstrate the versatility to use different propellants, have a large performance range capability, and provide thrust throttling. Research on advancing hybrid rocket propulsion has been ongoing since the early 1930s to maximize the potential of this type of rocket. The first hybrid rocket effort recorded came from Sergei P. Korolev and Mikhail K. Tikhonravov in 1933 with the GIRD-09. This rocket was 2.44 m in length, 0.18 m in diameter and was a sounding rocket (rocket carrying scientific instrumentation) that burned liquid oxygen with gelled gasoline. Their sounding rocket reached an altitude of 1500 m with a thrust of 500 N for 15s [1]. During the mid-1940's, the Pacific Rocket Society attempted to develop flight worthy hybrid rockets consisting of liquid oxygen and fuels such as wood loaded with carbon black, and rubber-based fuel [1]. After numerous designs, the Pacific Rocket Society successfully flew the XDF-23, reaching an altitude of 9 km [1]. The XDF-23 employed a LOX and a rubber-based fuel with an aluminum alloy nozzle.

However, research on hybrid rockets has been inconsistent throughout the years. Research was revived in the 1970s because of growing safety concerns with storing and handling of solid rocket motors. The 1980s and the 1990s introduced several hybrid propulsion programs that explored the development of large hybrid boosters such as the Joint Government/Industry Research and Development program and DARPA's Hybrid Technology Options Project [4]. The goals of the programs were to develop and demonstrate the feasibility of hybrid motors for space applications. In 2003, Scaled Composites and SpaceDev developed a nitrous oxide and HTPB hybrid motor for the sub-orbital SpaceShipOne. The propulsion system contained a four-port hybrid motor and successfully carried a pilot to 100 km [4]. However, the technology has yet to mature to the level of liquid bi-propellant or solid propellant rockets with most hybrid projects facing obstacles such as low regression rate, poor grain and web integrity, and low combustion efficiency.

1.1 Liquid Bi-Propellant Propulsion Systems

Chemical propulsion systems can be broken down to four categories: solid propellant, liquid bi-propellant, monopropellant, and hybrid systems. The liquid bi-propellant propulsion system consists of liquid or gaseous fuel and oxidizer that are pressure fed into a combustion chamber where they atomize, mix, and combust. Liquid propulsion systems are attractive because

of their high specific impulse, ranging between 290s to 450s, and high propellant density. In addition, liquid propulsion systems can be throttled by controlling the flow of both the fuel and oxidizer while maintaining oxidizer to fuel ratio.

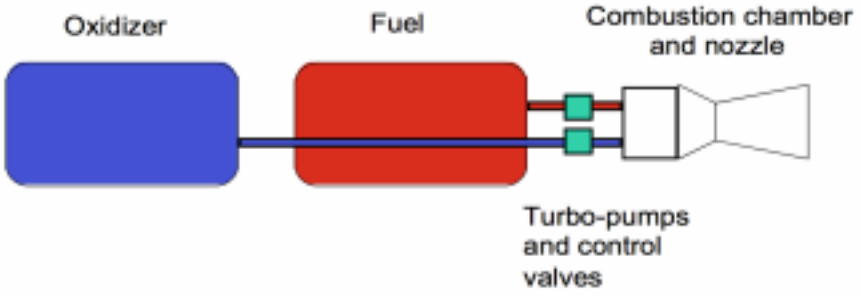

Figure 1.1: Schematic of a liquid bi-propellant rocket system [4]

However, the need to store both fuel and oxidizer separately adds complexity to the feed system. The plumbing required for the feed system becomes complicated and results in high cost for design and development and the use of cryogenic or hypergolic propellant exacerbates the system. In addition, the injector needed for the atomization and mixing of the propellants is complex and expensive. Though liquid propulsion systems can be throttled, the throttle ratios are limited due to reduced mixing at lower flow rates [4]. Another downside to these systems is that they are also known for combustion instabilities and high design and development costs.

1.2 SOLID PROPULSION SYSTEMS

Compared to liquid bi-propellant systems, solid propulsion systems are mechanically simpler because the fuel and oxidizer are premixed into a solid grain eliminating the need for a complex feed system. The complications with solid propulsion systems comes with the use of explosive mixtures for fuel grains. These fuel grains run the risk of accidental detonation and require stringent safety precautions for manufacturing, increasing the cost and complexity of the process.

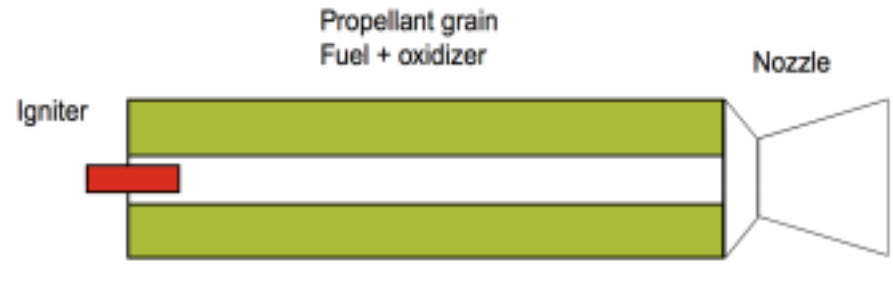

Figure 1.2: Schematic of solid propellant rocket system [4]

Solid systems commonly use less energetic oxidizers than liquid systems, which results in lower specific impulse. This lower specific impulse makes them less idea for primary propulsion systems. Cracks and imperfections within the fuel grain can cause uncontrolled combustion and explosion adding to the complexity of solid propellants.

1.3 HYBRID PROPULSION SYSTEMS

A hybrid rocket uses aspects of both solid and liquid propellants, typically with solid fuel and liquid or gaseous oxidizer. As previously stated, liquid propellant systems store the fuel and oxidizers separately and are mixed with an injector. This is different than solid propellants since the fuel and oxidizer are already mixed in a fuel grain that is located within the combustion chamber. Hybrid rockets, on the other hand, store the solid fuel grain within the combustion chamber and feed the oxidizer into the chamber which offer many unique attributes.

Hybrid rockets tend to be safer than liquid and solid rockets. The fuel grain is inert and reduces the risk of explosion or detonation while manufacturing, transporting, storing, and operating. For solid rockets, cracks or craters in the fuel grain can be catastrophic and potentially lead to an explosion, but are not problematic for hybrid rockets since combustion occurs down the port where it encounters the oxidizer flow [1].

Hybrid rockets also offer simplified throttling and shutdown. The motor can be throttled by controlling the oxidizer flow rate, which is simpler than liquid rockets that must synchronize flow rates of both oxidizer and fuel. The throttling capability of hybrids also allow for a smooth change in motor thrust over a wide range on demand. Termination of thrust can be achieved by simply terminating the flow of the oxidizer.

The simplicity and ease of manufacturing and handling of hybrid systems leads to lower overall operational costs. The need to only store the oxidizer reduces the plumbing and cryogenic fluid management associated with bi-propellant systems. The manufacturing of inert solid fuel grains can be done in a commercial facility without the stringent safety precautions required for solid propellants. These simplifications result in lower total operational costs.

However, hybrid rockets do face some downfalls. Hybrid systems suffer from low regression rates, or the velocity at which the fuel recesses normal to the fuel surface. In hybrid rockets, the flame front is an appreciable distance from the fuel grain surface and responsible for transferring the heat needed to burn the fuel, but lacks the exothermic chemical reaction seen in solid rockets from the combustion of both fuel and oxidizer [9]. This results in a lower regression rate compared to solid rockets and results in lower combustion efficiency since the combustion of oxidizer and fuel occurs in the flame zone and allows some oxidizer to pass through the chamber untouched. Regression rate also decreases as the port diameter increases, which causes a shift towards higher oxidizer to fuel ratios. This shift varies the specific impulse during steady-state operation.

Table 1.1: Performance of hybrid propellant, Pc = 500 psia and Pe = 14.7 psia [1]

Fuel	**Oxidizer**	**Optimum O/F**	**Sea Level Isp, s**	**c*, ft/s**
HTPB	LOX	1.9	280	5972
PMM ($C_5H_8O_2$)	LOX	1.5	259	5449
HTPB	N_2O	7.1	247	5264
HTPB	N_2O_4	3.5	258	5456
HTPB	RFNA	4.3	247	5219
HTPB	FLOX (OF_2)	3.3	314	6701
Li/LiH/HTPB	FLOX (OF_2)	2.8	326	6950
PE	LOX	2.5	279	5877
PE	N_2O	8.0	247	5248
Paraffin	LOX	2.5	281	5920
Paraffin	N_2O	8.0	248	5268
Paraffin	N_2O_4	4.0	259	5469
HTPB/Al(40%)	LOX	1.1	274	5766
HTPB/Al(40%)	N_2O	3.5	252	5370
HTPB/Al(40%)	N_2O_4	1.7	261	5509
HTPB/Al(40%)	FLOX (OF_2)	2.5	312	6582
Cellulose ($C_6H_{10}O_5$)	GOX	1.0	247	5159
Carbon	Air	11.3	184	4017

Carbon	LOX	1.9	249	5245
Carbon	N_2O	6.3	236	4992

Hybrid rockets commonly employ a high-energy oxidizer and polymeric hydrocarbon fuel. Hydroxyl-terminated polybutadiene (HTPB) is the widely-used fuel for hybrid motors because of its low surface tension and low viscosity of the melt layer, two favorable fuel properties for higher regression rates. As for the oxidizer, there is an ample motivation for the development and use of storable oxidizers such as nitrous oxide, hydrogen peroxide, hydroxyl ammonium nitrate, and other energetic liquids. Table 1.1 details the performance characteristics of these storable oxidizers and hydrocarbon fuels.

1.4 HYDROXYL AMMONIUM NITRATE

There has been a recent push for the advancement of ionic liquid monopropellants to replace the commonly used monopropellant, hydrazine. Hydrazine in its various forms is an extremely good monopropellant. It has a specific impulse of 230s, extremely high reactivity with iridium coated catalysts [3], relative stability, and clean exhaust gases. However, hydrazine is an extremely toxic and corrosive propellant. Due to the toxicity of hydrazine, the advancement of aqueous energetic ionic liquids has been investigated recently. The National Institute for Occupational Safety and Health classifies hydrazine and its derivatives as a toxic compound and a human carcinogen that can cause severe nausea, and other harmful effects if hydrazine comes in contact with skin or is inhaled or swallowed [19]. Aside from the health hazards associated with hydrazine, the high vapor pressure of the propellant makes it difficult to store in comparison of the other monopropellants listed in Table 1.2.

Table 1.2: Properties of commonly used monopropellants [3,17]

Chemical	**Density (g/mL)**	**Isp (sec)**	**Vapor Pressure @ 293 K (psia)**
Hydrazine	1.01	230	0.203
Hydrogen Peroxide	1.45	165	0.097
LMP-103S	1.24	252	~
AF-M315E	1.46	266*	~

*Theoretical Isp

The disadvantages of hydrazine ushered in the Green Propulsion Infusion Mission (GPIM) for the development of green propellant to replace hydrazine and other toxic propellants. This initiative has resulted in an Air Force developed, HAN-based monopropellant AF-M315E. The green monopropellant surpasses both conventional monopropellants, hydrazine and hydrogen peroxide, with a higher density, higher specific impulse, and is less toxic and relatively safe to handle. Specific impulse is the total impulse per unit weight of a propellant and is an important indication of the performance of a propulsion system [18]:

$$I_{sp} = \frac{F}{\dot{m}_p g_0} = \frac{C_F c^*}{g_0} \tag{1.1}$$

where C_F is the thrust coefficient and c^* is the characteristic velocity. A higher specific impulse indicates the chosen propellant mass can generate more thrust per unit mass, which can be critical depending on the vehicle for the mission.

AF-M315E is a maturing monopropellant currently used in small space system propulsion systems with little known implementation in hybrid rockets. Many hybrid rockets have operated on HAN, a significant component of AF-M315E, and offer an insight to the potential performance of green propellant based hybrid rockets. Hydroxyl ammonium nitrate is a salt often diluted with water to produce an energetic ionic liquid suitable as rocket propellant. Investigation of HAN is motivated by the relative high density specific impulse, environmentally friendly exhaust products, and performance potential. Table 1.3 displays the performance of various oxidizers with HTPB in a hybrid motor configuration. Of these oxidizers, liquid oxygen is the most common oxidizer used for hybrid rockets because it provides the highest specific impulse [8].

Table 1.3: Performance comparison for various oxidizers with HTPB, PE, and DCPD, P = 1000 psi, sea-level expansion. [8]

Propellant Combination	Optimal O/F	ρ_f (g/cm^3)	ρ_{ox} (g/cm^3)	ρ_b (g/cm^3)	I_{sp} (s)	$\rho_b I_{sp}$ (g*s/cm^3)
LOX/HTPB	2.3	0.92	1.14	1.06	298.4	316
90% HP/PE	7.8	0.90	1.39	1.31	266.1	348
98% HP/PE	7	0.90	1.43	1.33	275.7	367
98% HP/DCPD	6.2	1.01	1.43	1.35	277.5	375
95% HAN/HTPB	9.6	0.92	1.68	1.56	251.1	392
N_2O/HTPB	7.4	0.92	1.98	1.74	266.4	463

Liquid oxygen (LOX) and HTPB hybrid motors are shown to have a significantly higher specific impulse of the motors in Table 1.3. In comparison, hydrogen peroxide (HP), HAN, and nitrous oxide show advantages in bulk density that results in a competitive density specific impulse:

$$I_d = \rho_b I_{sp} \tag{1.2}$$

where ρ_b is the bulk density of the propellants and I_{sp} is the specific impulse. In addition, aqueous solutions of HAN display properties of an ideal liquid oxidizer because it is liquid at room temperature, non-toxic propellant that eliminates stringent safety requirements, stable over long term storage, and possess low viscosity [2]. The study by Biddle and Sutton calculated the theoretical performance of 80% and 85% HAN concentrations with an 80% HMX polybutadiene fuel grain illustrates a competitive theoretical specific impulse, 275.8 sec, compared to the liquid oxygen and HTPB combination [2]. However, there is little published work on HAN based hybrids and none available using AF-M315E.

1.5 PROJECT OVERVIEW

Hybrid rocket propulsion is promising technology that shows the potential of combining the advantages of both liquid and solid rockets. However, hybrid rocket motors suffer from low regression rate and immature technology that hinders its practicality. The suggested use of AF-M315E and HTPB as the oxidizer and fuel offers the potential for developing high impulse hybrid motors with low developmental and production costs.

The project's main objective is to develop a small-scale system to measure the regression rate and build a regression rate prediction model. To achieve this objective, an existing test apparatus was modified to test HTPB with gaseous oxygen along with the predicted decomposition gases of HAN. Gaseous oxygen and HTPB was initially tested to validate the system and to serve as a baseline to assess the performance of the HAN and AF-M315E decomposition gases.

1.6 PROJECT RELEVANCE

With the lack of published work on the use of HAN based propellants in hybrid rockets, this study provides insight on the performance of hybrid motors using HAN. This study provides regression rate data and model for HAN that will serve as a baseline for future work aimed at improving the regression rate for the propellant. This work also furthered the Center for Space

Exploration and Technology Research's capability of developing and testing hybrid rockets along with the applications of green monopropellants.

Chapter 2: Background

2.1 Regression Rate

The fuel regression rate for hybrid and solid propellant systems is the most important value for the motor design and performance prediction. Regression rate is the rate at which the fuel recesses normal to the fuel surface, or the rate at which the solid-phase fuel is vaporized and converted to the gas phase. For solid propellant systems, the regression rate, or burn rate, is controlled by the chamber pressure:

$$r = ap_c^n \tag{2.1}$$

where r is the burn rate, a is an empirical constant influenced by the ambient fuel grain temperature, p_c is the chamber pressure, and n is the combustion index that describes the influence of the chamber pressure on the regression rate [18]. As can be seen by the burn rate equation, the regression rate for solid propellant motors are highly sensitive to the chamber pressure. Any fluctuation on chamber pressure can significantly influence the regression rate.

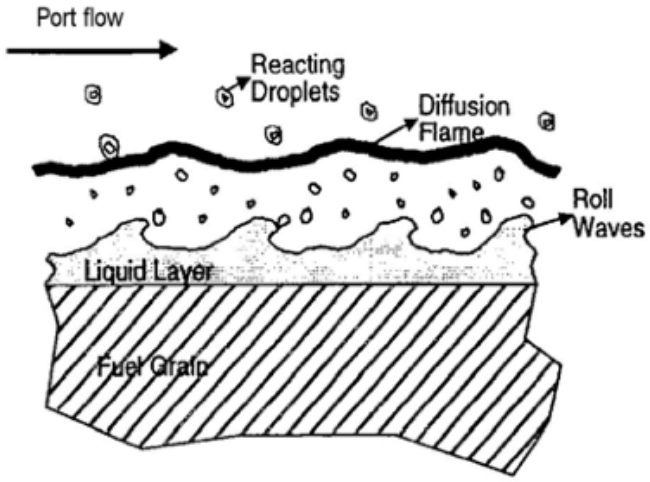

Figure 2.1: Illustration of the internal ballistics of hybrid motors [15].

The regression rate for hybrids differs from solid systems and it is important to understand the combustion process in hybrids to properly understand the regression rate. In hybrid rockets, a

solid fuel grain is contained within the combustion chamber while the liquid or gaseous oxidizer is injected into the fuel grain port at a high Reynolds number. After ignition, a boundary layer develops over the fuel surface and the combusted gas is carried within the boundary layer to the surface of the fuel. This boundary layer is assumed to be turbulent along the full fuel grain because of the oxidizer's high Reynolds number and the surface mass addition from the fuel ablation is known to reduce the transitional Reynolds number for turbulent flow. In addition, a thin diffusion flame layer forms in the boundary layer. The heat conducted from the flame zone causes the fuel to pyrolyze, either resulting in a thin melt layer developing on top of the fuel or charring and depolymerization (if the fuel is a polymer such as HTPB). Droplets of fuel are entrained from this melt layer and transported through the flame zone where they vaporize, mix with the oxidizer and burn. This process is illustrated in Figure 2.1.

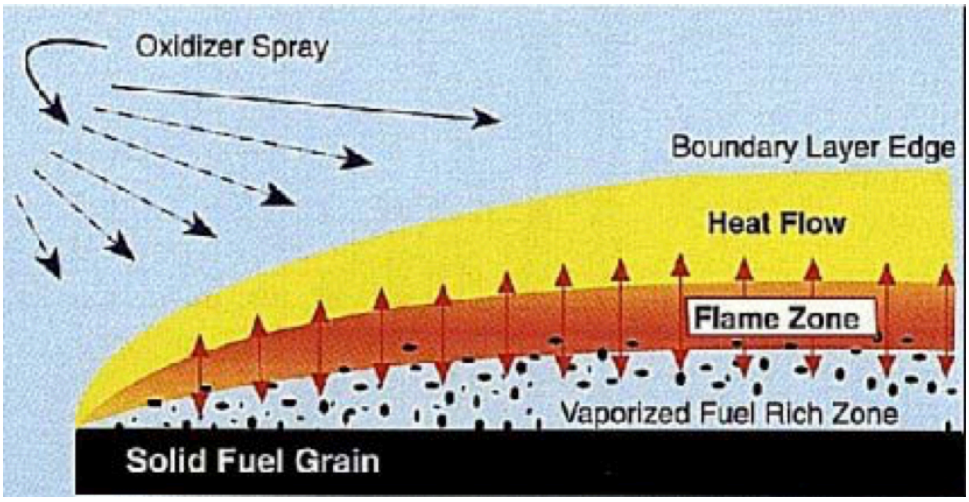

Figure 2.2: Illustration of the boundary layer developed in a hybrid motor [15].

The regression rate for hybrids differ from solid rockets and is primarily controlled by the rate at which heat is delivered to the fuel surface. A simplified approach was taken by Marxman and Gilbert. These authors analyze the hybrid regression rate based on the heat transfer in a turbulent boundary layer. This approach assumes the boundary layer is comprised of two zones, one above the flame where the flow is oxidizer rich and one below the flame where the flow is fuel rich, which can be seen in Figure 2.2. The zone below the flame is the effective boundary layer for the heat transfer to the wall and since the regression rate is proportional to this heat flux:

$$\rho_f \dot{r} = (\rho v)_w = \frac{\dot{Q}_w}{\Delta H} \tag{2.2}$$

where ρ_f is the density of the solid fuel, $\dot{r}$ is the linear regression rate of the fuel surface, $(\rho v)_w$ is the gas phase mass flux at the fuel surface, $\dot{Q}$ is the heat transfer per unit area to the wall, and ΔH is the effective heat of gasification of the solid fuel [14].

However, Marxman's theory was developed for a slab configuration fuel grain compared to a cylindrical configuration most practical motors employ today. This leads to an over prediction of the regression rate since the theory predicts a high averaged mass flux and higher dependence on axial location [13]. Instead, with Marxman's regression rate law in mind, an empirically determined averaged regression rate law is used:

$$\dot{r} = a\bar{G}_{ox}^{n}\bar{x}^{m} \tag{2.3}$$

where a is the regression rate coefficient, n and m are propellant dependent constants, and $\bar{G}_{ox}$ is the average mass flux.

Equation 2.1 shows the regression rate's independence of chamber pressure for hybrid rockets. This is true for low total mass fluxes (<49.3 kg/m^{2}s) which was proven from studies performed by Smoot and Price [10]. Smoot and Price performed over 150 small scale experiments and defined three regions of regression rate dependence outline in Figure 2.2. For low mass fluxes, the regression rate is controlled by the heat transferred from the flame zone and the mass flux. For medium mass fluxes, the regression rate is controlled by both the mass flux and the chamber pressure, governed by the following equation:

$$\dot{r} = \frac{aG^{0.8}bp^{n}}{aG^{0.8} + bp^{n}} \tag{2.4}$$

where p is chamber pressure, G is total mass flux and $a, b,$ and n are empirical constants [10]. For high mass flux, regression rate is entirely dependent on chamber pressure (Equation 2.1). Smoot and Price concluded that the dependence on pressure were a result of either gas-phase oxidizer-fuel reactions or heterogeneous reactions between oxidizer and fuel at the surface [17].

Regression rate is critical for the sizing of a fuel grain for a desired thrust level, thus prompting the need for improvement. A lower regression rate requires a larger grain surface area to provide the required thrust, which leads to a low volumetric fuel loading and density. Therefore,

the lower regression rate results in the need for a longer fuel grain adding to the overall weight and cost of the system.

2.1 HAN DECOMPOSITION

Little published work is available on the properties or the decomposition process of AF-M315E due to its proprietary nature. However, publication on the decomposition of HAN is available and offers insight on the decomposition process of AF-M315E. Mentioned previously, hydroxyl ammonium nitrate (HAN) solutions show promise with high density specific impulse and environmentally friendly exhaust products. However, systems employing aqueous HAN solutions exhibit operational problems such as combustion instabilities and unreliable ignition. To alleviate the operational issues of HAN, studies have been conducted to characterize the combustion behaviors of HAN. More so, studies have been conducted to learn the thermal and catalytic decomposition process of aqueous HAN solutions.

Thermal and catalytic decomposition studies were performed by Courthéoux, et al on various HAN concentrations to characterize the monopropellant [5,6]. A batch reactor was used to heat up solutions of HAN with and without a Platinum based catalyst and thermogravimetric analysis and differential thermal analysis were used to determine the onset temperature of decomposition, concentration of HAN solution at decomposition, and the exothermic peak. The solution under thermal decomposition exhibited an initial endothermic peak due to the evaporation of water followed by an exothermic peak resulting from the decomposition of HAN. Figure 2.3 details the thermal decomposition of a 40% HAN solution in the batch reactor where the thermal decomposition temperature of 135°C was observed for the solution. It should be noted that the decomposition of HAN can only proceed once all the water has been evaporated, leaving pure HAN.

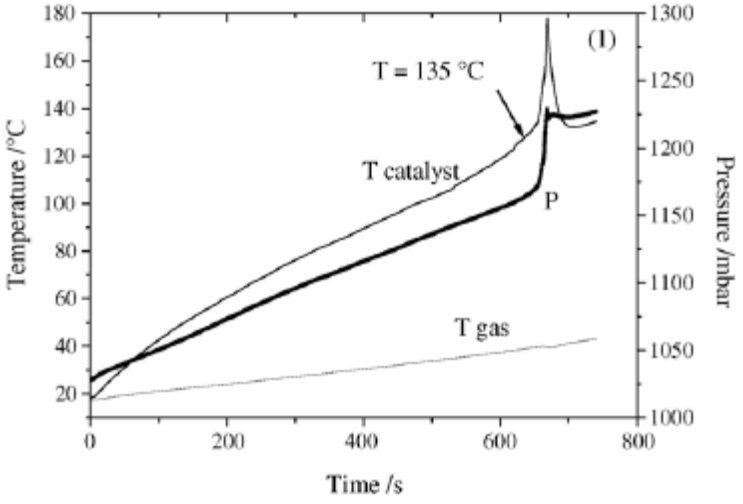

Figure 2.3: Thermal decomposition of 40% HAN solution [5,6]

A similar experiment was designed to study the effect of a platinum coated alumina catalyst on the decomposition of HAN. A batch reactor was used to heat up the solution with the catalyst and thermogravimetric and differential thermal analysis were used to determine the onset temperature of decomposition. As displayed in Figure 2.4, the decomposition temperature of HAN in the presence of a catalyst is lower, 107°C.

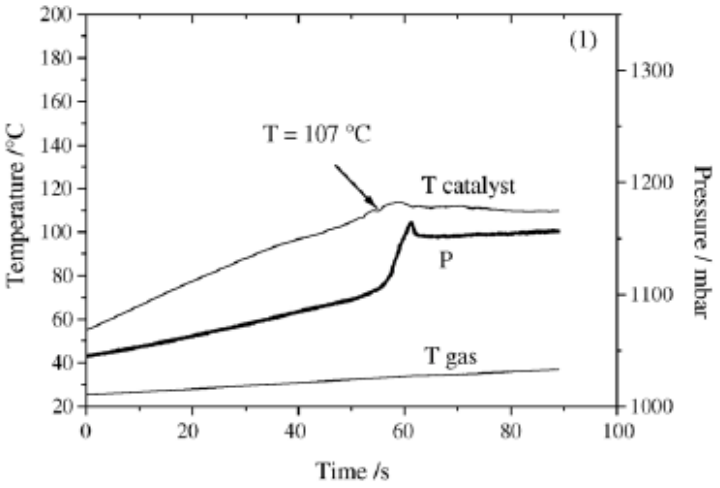

Figure 2.4: Catalytic decomposition of 40% HAN solution [5,6]

In addition to the thermal analysis for the decomposition process, studies have been performed to identify the products of the decomposition process. Lee and Litzinger developed an experiment to measure concentrations of the decomposition species of various HAN solutions using Fourier transform infrared spectroscopy. A sample of aqueous HAN solution was placed in a holder, heated to a set temperature, and a FTIR spectrometer was used to obtain the infrared spectrum emissions of the decomposition species. From their experiment, the decomposition process was characterized by [11]:

1) An induction period followed by H_2O evaporation
2) The rapid evolution of N_2O, NO, and HNO_3
3) Formation of NO_2

The major decomposition products detected were H_2O, N_2O, NO, and NO_2 with traces of HNO_3[11,15], which can be seen in Figure 2.5. To understand the effect of water on the thermal decomposition process, various HAN concentrations were tested and showed an increase in induction time and slower evolution of decomposition gases as the water concentration increased.

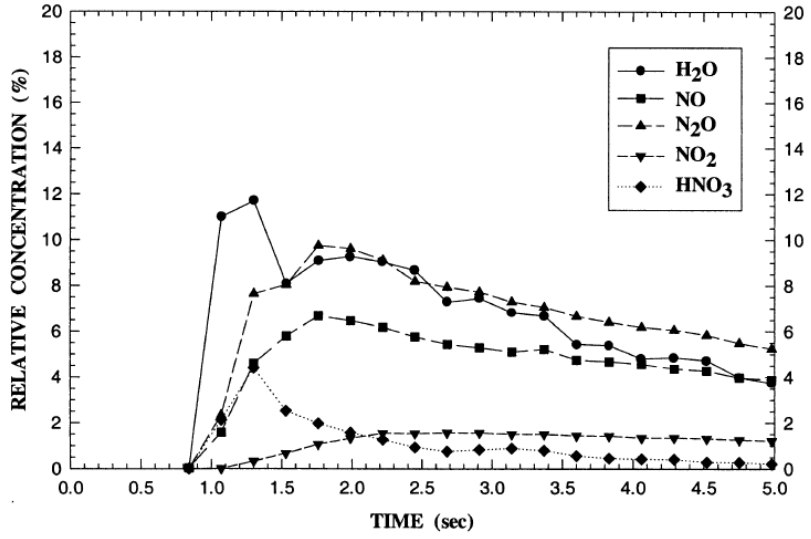

Figure 2.5: Evolution of species concentrations during thermal decomposition of 13 M HAN solution at 180°C [11].

The resulting reaction mechanism identified from the study is [12]:

$$HAN + H_2O \rightarrow NH_2OH + HNO_3 + H_2O$$
$$NH_2OH + HNO_3 \rightarrow HONO + HNO + H_2O$$

$$NH_2OH + HONO \rightarrow N_2O + 2H_2O$$

$$2HNO \rightarrow N_2O + H_2O$$

$$NH_2OH + HNO \rightarrow N_2 + 2H_2O$$

$$3HONO \rightarrow 2NO + HNO_3 + H_2O$$

$$HNO + HNO_3 \rightarrow 2NO + H_2O$$

$$HONO + HNO_3 \rightarrow 2NO_2 + H_2O$$

The NASA computer program CEA (Chemical Equilibrium with Application) was used to supplement the HAN decomposition products found through literature. CEA is a program that calculates the chemical equilibrium products and thermodynamic and transport properties of reactants. For this study, 95% HAN solution was selected for the oxidizer (refer to Appendix B for CEA input file), resulting in the following decomposition products:

Table 2.1: HAN decomposition products from CEA

Species	**Formula**	**Mass Fraction**
Oxygen	O_2	0.29591
Nitrogen	N_2	0.26957
Steam	H_2O	0.38657
Nitric Oxide	NO	0.01610

The study of HAN thermal and catalytic decomposition is important because it gives details about the behavior of AF-M315E main components. When using AF-M315E in a hybrid motor, the propellant will likely be thermally or catalytically decomposed prior to being injected into the combustion chamber. The reaction mechanism identified from these decomposition studies forecast the products that will be injected into the combustion chamber and interacting with the fuel along with the path the propellant may take in decomposing.

Chapter 3: Experimental Design

3.1 TEST SETUP

To benchmark the experimental measurements of the regression rate, a series of tests were performed with gaseous oxygen and HTPB. The validation of the experimental technique was done using gaseous oxygen and HTPB then this same setup used to compare the results of simulated HAN decomposition gases with HTPB. To achieve the goal, the system that was used is required to:

- Inject the oxidizer at the desired flow rates
- Ignite the oxidizer and fuel
- Secure the HTPB fuel grain within the holder
- Measure inlet and outlet gas temperature
- Operate the system safely

Figure 3.1 and Figure 3.2 show the schematic and assembly of the test rig for the gaseous oxygen and HTPB experiment. Each system contains five components: the delivery and purge units, fuel grain, fuel grain holder, ignition, and the exhaust systems. The delivery system feeds the oxygen and carbon dioxide through tubing to the inlet of the fuel grain holder. The system also provides methane to the ignition system. The fuel grain secures the fuel grain and connect to a pre-existing setup. An exhaust system was installed to capture and vent the exhaust products during testing.

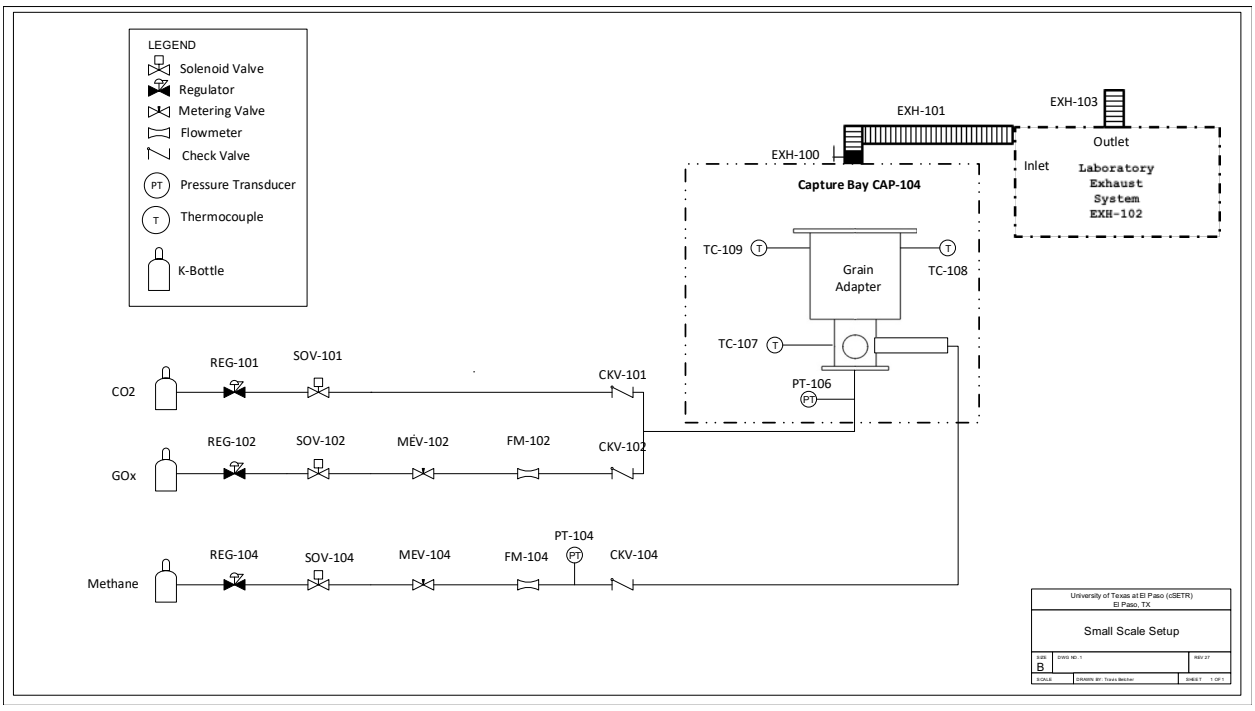

Figure 3.1: Gaseous oxygen and HTPB schematic

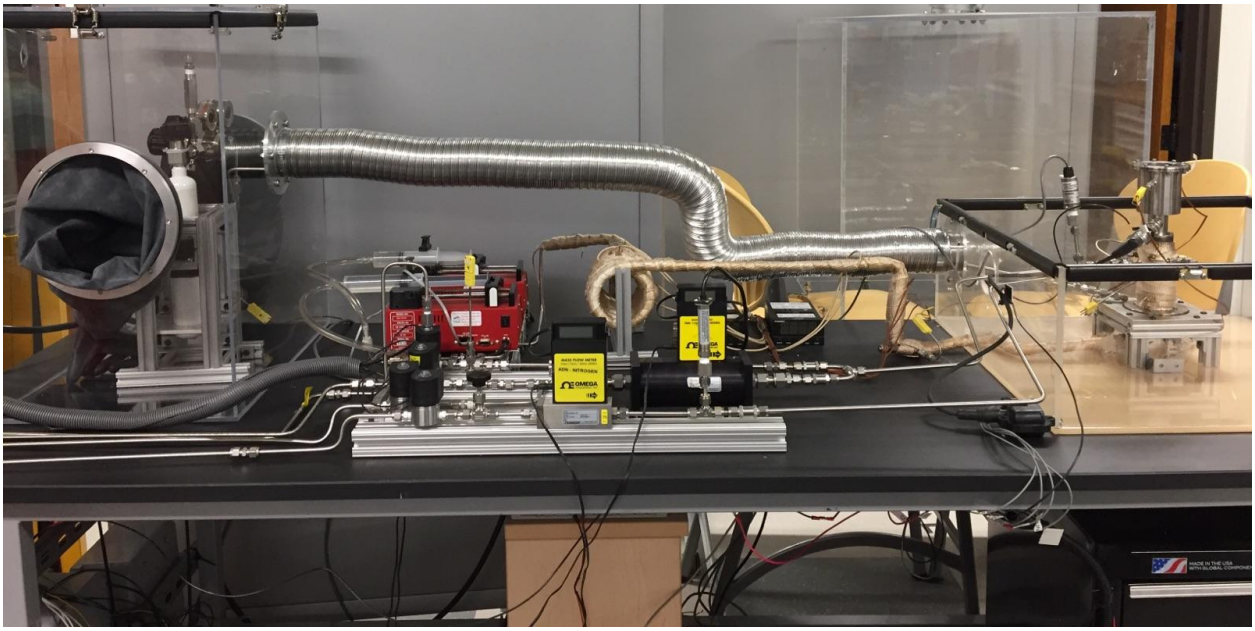

Figure 3.2: Small-scale GOx and HTPB test setup

Once the test rig was validated, additional feed lines were installed to represent the HAN decomposition products. Figure 3.3 and Figure3.4 show the schematic and assembly of the HAN decomposition test rig. The modified system contained feed lines for oxygen, methane, and carbon

dioxide. In addition, a steam generator was installed consisting of a heated coil, two syringe pumps, and a water tank. A line for nitrogen, Table 2.1, was also added to the system.

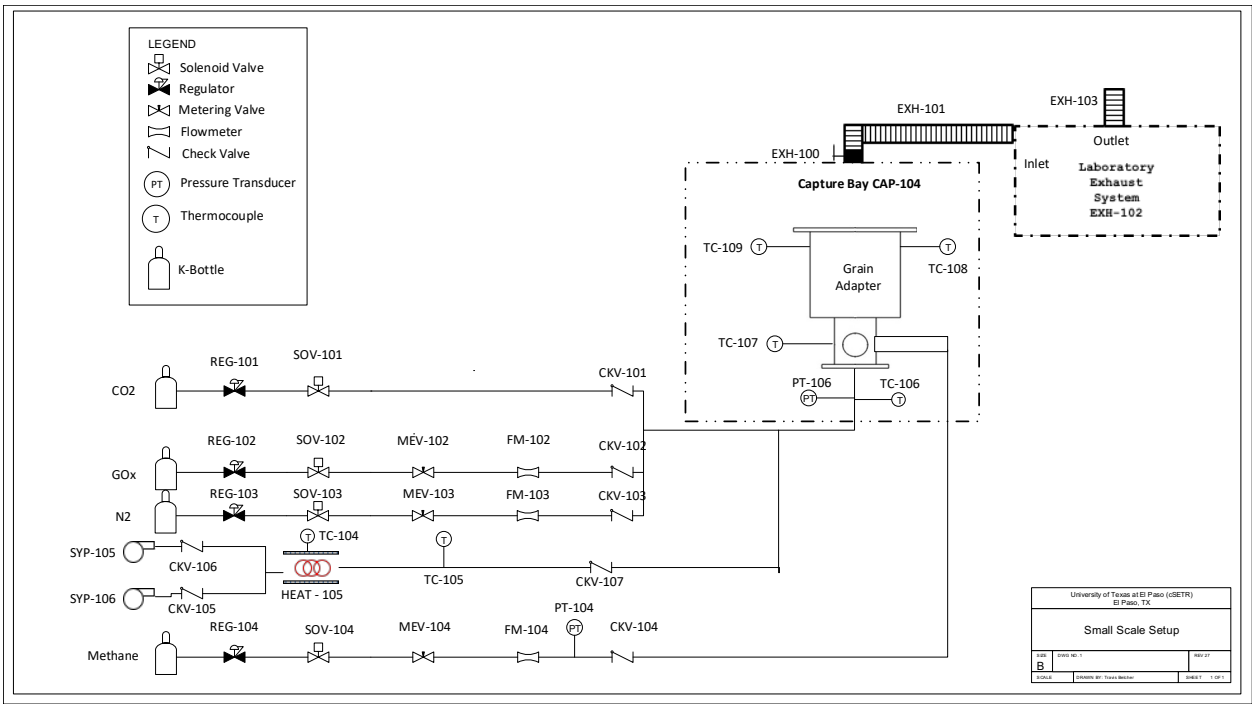

Figure 3.3: HAN decomposition gases and HTPB test rig schematic.

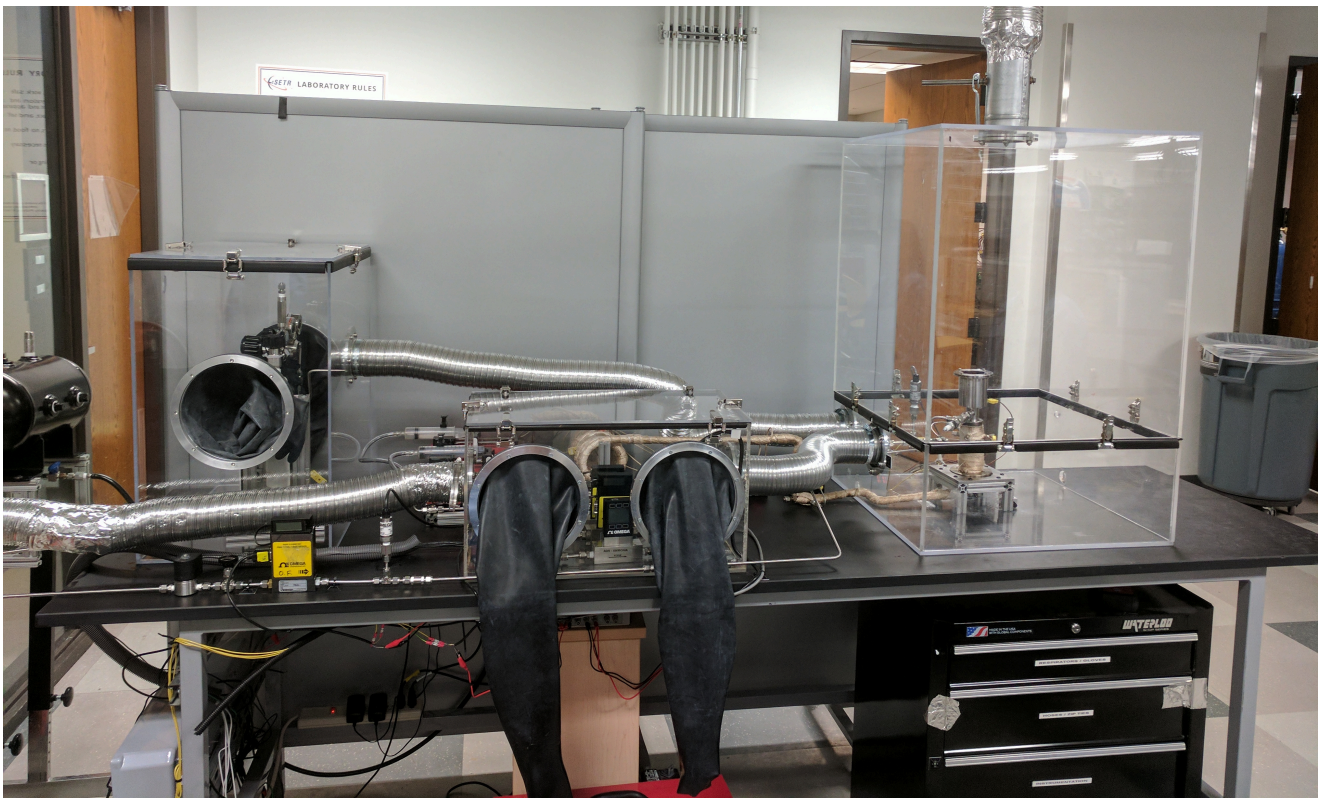

Figure 3.4: Fully integrated HAN decomposition and HTPB test rig.

The following sections describe the design, analysis, and manufacturing of the experimental system for regression rate measurements of gaseous oxygen and HAN decomposition gases with HTPB.

3.1.1 Delivery and Purge System

The delivery system is designed to deliver oxidizer and carbon dioxide to the inlet of the fuel grain holder and deliver methane to the ignition system. Each gas is contained within a K-bottle and is regulated using a two-stage pressure regulator. The pressure regulator is connected to a line leading to an isolation valve, Figure 3.6. This allows the test conductor to remotely initiate and terminate the flow of each gas. For the oxygen and nitrogen feed lines, a flow meter, Figure 3.7, proceeds the isolation valve and measures the gas flow. To prevent backflow, a check valve was installed in each gas feed line. For the methane feed line, the isolation valve is followed by a metering valve to allow flow control and then proceeded by a flow meter like Figure 3.7. The permissible exposure limit (PEL) for nitric oxide is low and presents hazardous risks to the test conductors. To reduce exposure and risk, the oxidizer feed lines and the fuel grain holder were

placed within capture bays that are connected to the exhaust, venting the system. These capture bays can be seen in Figure 3.4.

(a)

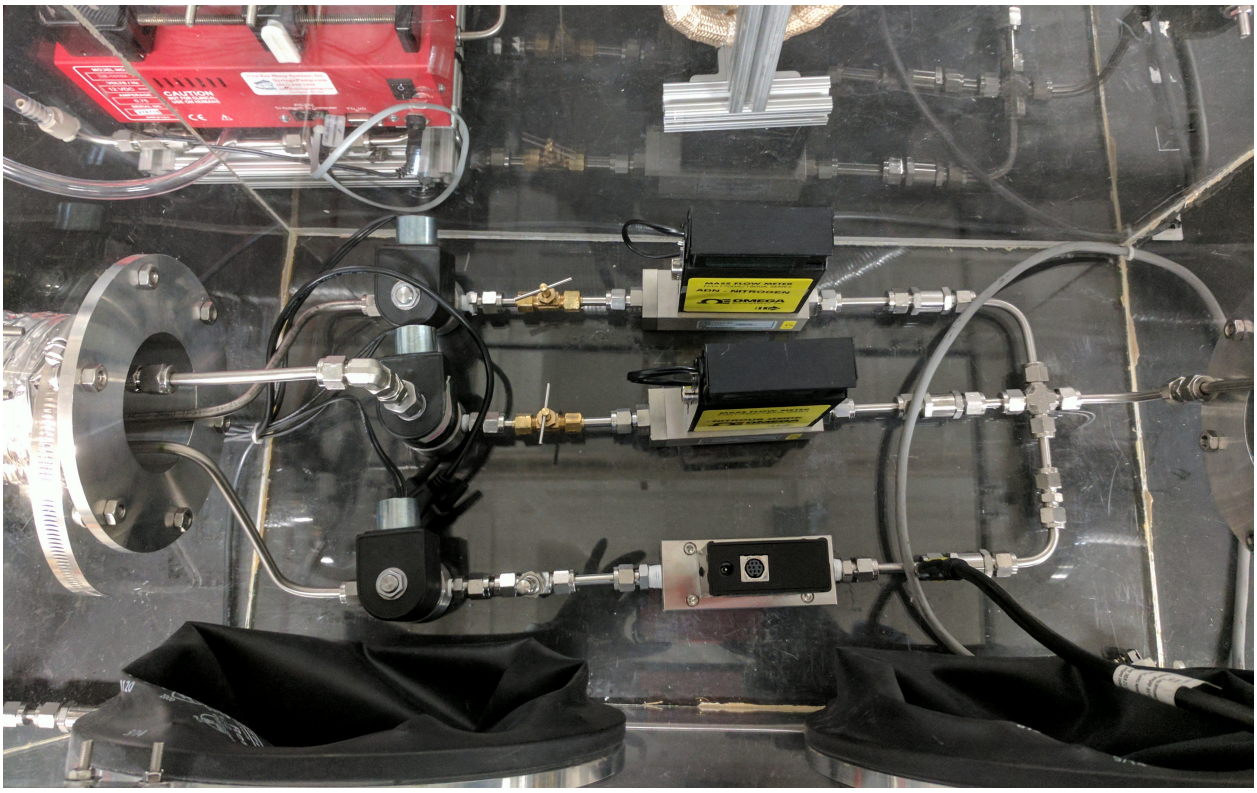

(b)

Figure 3.5: Delivery system for (a) gaseous oxygen and (b) HAN decomposition test setup.

Figure 3.6: Normally closed isolation valve used for oxygen.

Figure 3.7: Omega FMA 1700A/1800A series mass flowmeters used to monitor flowrates.

The delivery system for the oxygen and HTPB testing also contains carbon dioxide to extinguish the motor after each test and purge the system. Unlike the normally closed solenoid valve used for the oxygen and methane feed lines, the carbon dioxide feed line contains a normally open solenoid valve. This allows the purge system to introduce carbon dioxide in the event of power loss or unexpected ignition, acting as a fail-safe. A check valve follows the isolation valve to prevent backflow. Nitrogen replaced carbon dioxide for the purge system for the HAN decomposition and HTPB testing.

Figure 3.8: New Era syringe pump used to inject water into heated coil.

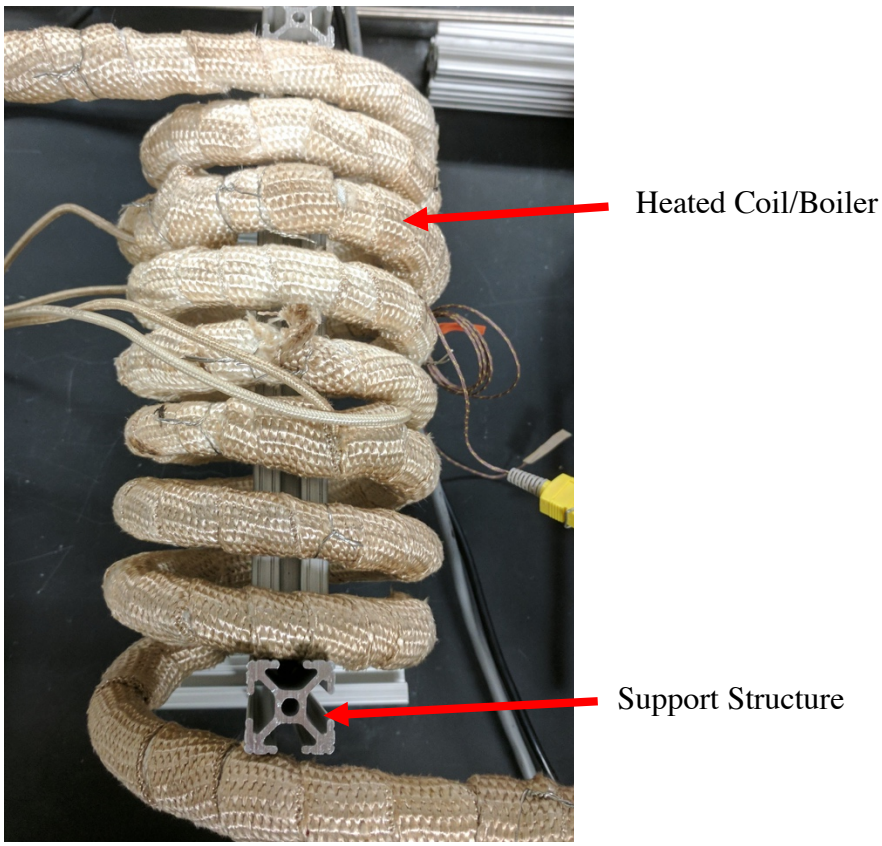

Figure 3.9: Heated coils used to evaporate water to generate steam.

Since steam is a decomposition product for HAN, a steam generator system was installed to inject and evaporate water. The system uses two syringe pumps, Figure 3.8, to inject the appropriate amount of water to the heated coil shown in Figure 3.9. The coil is wrapped with Omega high temperature heat tape to heat the injected water to 180°C and evaporate and heat the steam to the expected decomposition temperature. Thermocouples are placed in-between the heat rope and along the line to monitor the temperature of the coil and the water flow. Check valves are also installed after the syringes to prevent backflow.

3.1.2 HTPB Fuel Grain

A key component of the small-small scale setup is the fuel grain itself. The design and development of the fuel grain was required to be:

- Safe to manufacture in-house
- Simple
- Consistent

- Allow easy alteration

Since the regression rate data obtained from testing was compared to literature, the commonly used central port diameter of 1.1 cm was chosen. The regression rate for hybrids depends on the oxidizer mass flux and is the key parameter used for determining the web thickness of the grain. A Mass flux between 0.2 to 0.64 g/cm^2-s was chosen because they were used previously in a study conducted by DeLuca, et al [7]. The study by DeLuca, et al investigated the regression rate of gaseous oxygen and HTPB of a lab-scale cylindrical motor, with a port diameter of 1.8 cm and a length of 3 cm, for mass fluxes ranging between 0.7 to 4 g/cm^2-s [7].

The maximum expected regression rate of 0.027 cm/s was calculated using the regression rate model obtained by DeLuca, et al for gaseous oxygen and HTPB [7]:

$$\dot{r}_{HTPB} = 0.055 G_o^{0.687} \tag{3.1}$$

where the mass flux is in kg/m^2-s and the regression rate in mm/s. The minimum web thickness, the thickness of the grain from the burning surface to the casing, of 1.62 cm was determined using this theoretical regression rate and test duration of 30 seconds. A web thickness of 2 cm was selected to prevent over-burning the grain in the event the actual regression rate is higher than expected. A stainless-steel sleeve was used to enclose the fuel grain because the interior of the sleeve was rough enough for the uncured HTPB to adhere as well as being flame retardant.

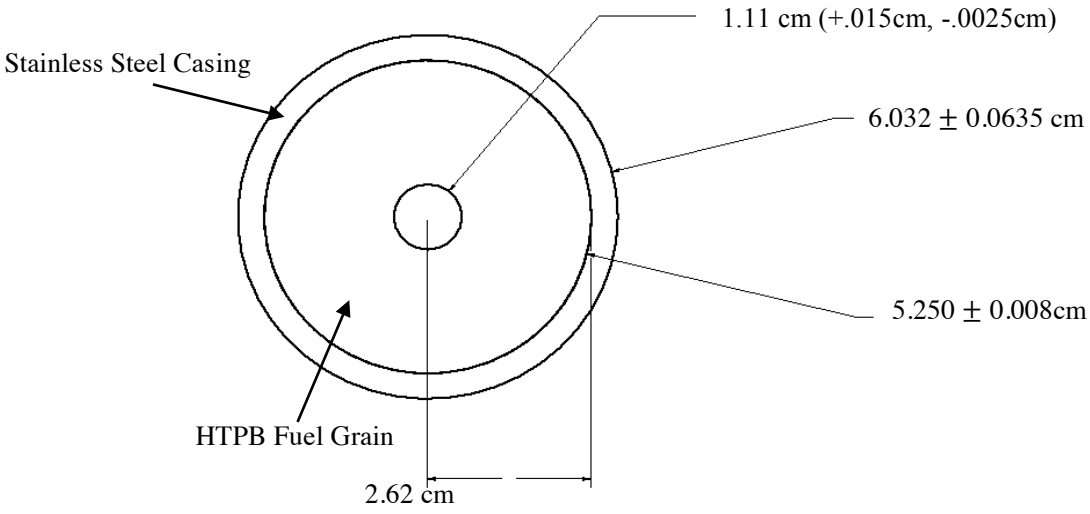

Figure 3.10: Dimensions of the HTPB fuel grains.

Development of the HTPB fuel grains required a simple and safe procedure to produce consistent fuel grains, while allowing for easy alterations. The procedure involves three chemicals: the HTPB resin R-45, the curing agent isophorone diisocyanate (IPDI), and carbon black powder. Each component is weighed, mixed in a beaker, and then placed in a vacuum chamber to remove any entrained air bubbles in the mixture. After the mixture is exposed to vacuum, the mixture is poured into individual motor molds and placed into the vacuum chamber again to remove residual entrained air bubbles. The motors are then cured in ambient conditions for 24 hours before placing them into an oven at 63°C to cure for an additional seven days.

Figure 3.11: Fully cured and perforated HTPB fuel grain.

The mixing procedure takes about 150 minutes with the final product as shown in Figure 3.11, each motor weighing roughly 100 g. Carbon black powder was added to the fuel grain mixture to reduce the heat radiated from the burning surface throughout the entire grain. The thermal penetration depth is significant because the subsurface layers can cook for a long time, altering the properties of the fuel and affecting the regression rate if the penetration depth is great [14]. Depending on the fuel, the altered fuel properties can result in sizable liquid droplets that burn poorly, consequently lowering the combustion efficiency.

3.1.3 Fuel Grain Holder

In addition to manufacturing fuel grains, a fuel grain holder was built to properly secure the grains during testing. The design of the holder is not only driven by the constraints of the fuel grain, but also the constraints of the system. Therefore, the following design criteria were used for the fuel grain holder:

- Contain the fuel grain throughout testing duration
- Allow access to fuel grain
- Attach to existing burner support
- Include ports for thermocouples
- Adapt an ignition system

As previously mentioned, the fuel grain's outer diameter of 6.032 cm and height of 5.08 cm drives the grain holder's chamber design. Therefore, the chamber inner diameter was designed to be 6.25 cm with a height of 7.62 cm, shown in Figure 3.12. The height of the inner chamber also encapsulates the design of the end cap that is needed to secure the fuel grain in the chamber during testing. Since the end cap is secured to the holder with eight bolts, the fuel grain is easily accessible for removal and replacement.

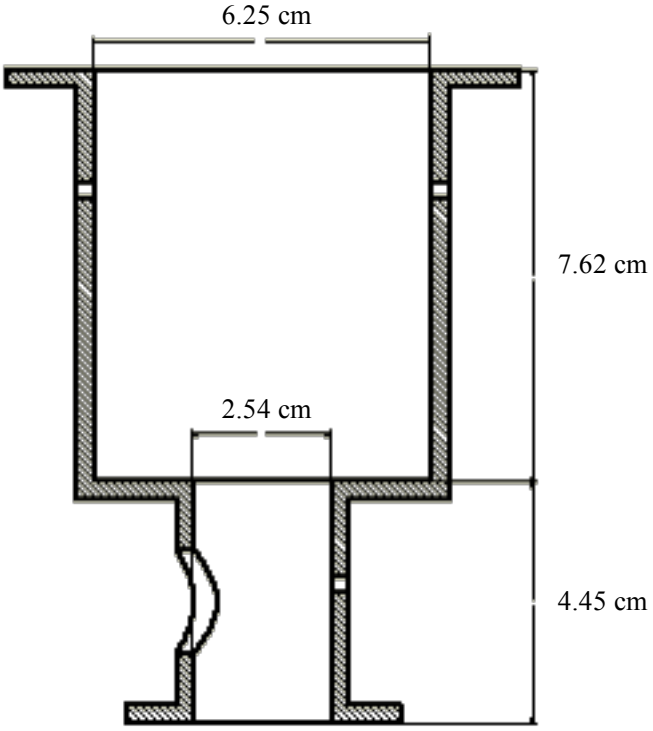

Figure 3.12: Fuel grain holder dimensions.

The use of an existing setup required the inlet of the fuel grain holder to be adaptable. The fuel grain holder inlet was designed to flange onto the burner support and is secured with four bolts, shown in Figure 3.13. The burner support is used to introduce the oxidizing gases from the feed system to fuel grain holder at the desired mass flow rates. The burner contains four channels for the oxidizers that lead to a mixing chamber and is outlined in the drawing in Appendix A. There is also a central channel in the burner support that is used to introduce steam.

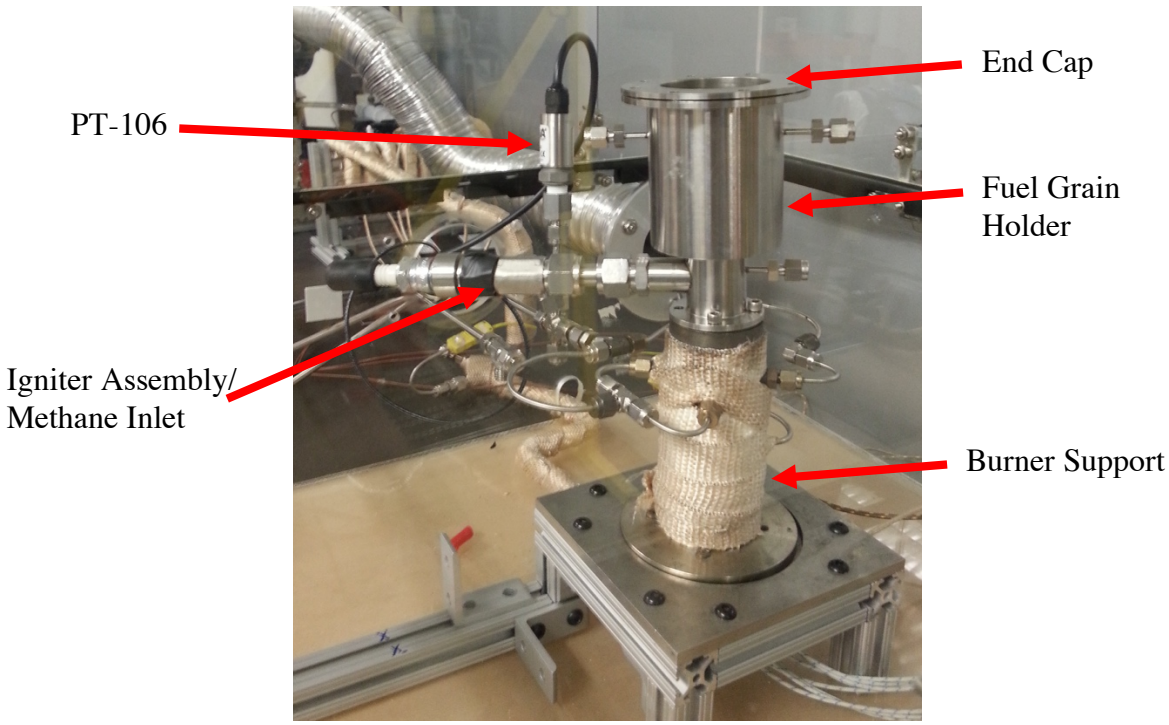

Figure 3.13: Fuel grain holder assembly and installation.

The holder contains three thermocouples that are used for measuring the exhaust plume temperature and the igniter diffusion flame temperature. Shown in Figure 3.14, thermocouples TC-109 and TC-108 monitor the plume temperature and displays a temperature rise when the fuel grain combusts, while thermocouple TC-107 monitors the igniter flame temperature. The thermocouple ports consist of tube to stem compression fittings that were laser welded to the Inconel holder, which allows the use of either thermocouples or pressure transducers, depending on the desired data.

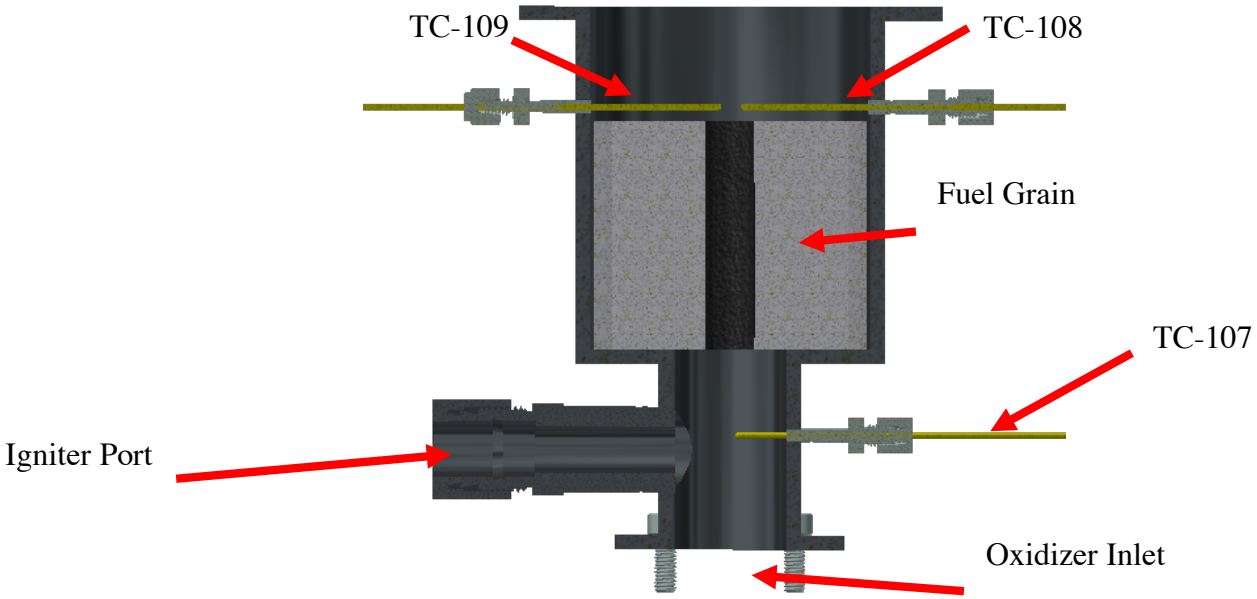

Figure 3.14: Fuel grain holder assembly illustrating thermocouple placements

3.1.4 Methane Ignition System

The fuel grain holder also needed to adapt an ignition system. The ignition system is critical for the hybrid motor system as it creates a methane diffusion flame that provides energy to initiate pyrolysis of the fuel grain and ignite the motor. For HTPB, the ignition system needs to provide enough energy to depolymerize the hydrocarbon and subsequently vaporize the resulting monomers. For this study, the ignition system utilizes a handheld igniter and a small flow, 0.03 g/s, of methane to provide enough energy for ignition and pyrolysis of the fuel grain.

Figure 3.15: Handheld igniter

Methane is introduced through the T-connection shown in Figure .16. A handheld igniter is used to ignite the 0.03 g/s flow of methane, creating a diffusion flame that will be used to heat the gaseous oxygen and initiate combustion with the fuel grain.

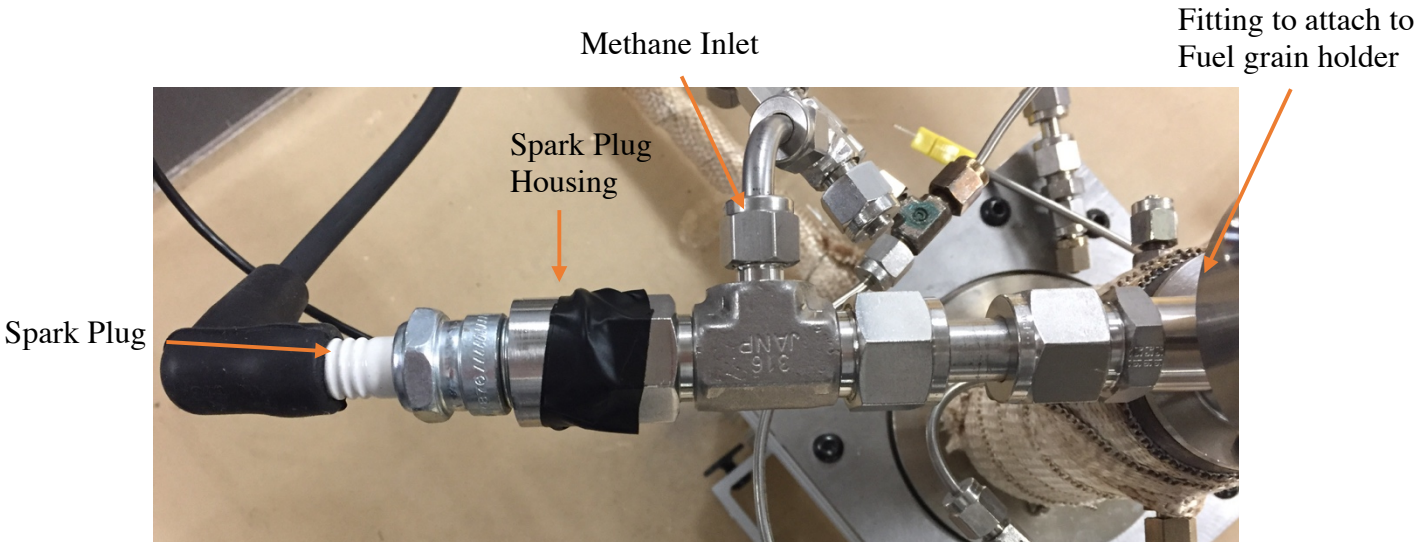

Figure 3.16: Igniter assembly

3.1.5 Exhaust System

The final component of the small-scale system is the exhaust system, designed to capture and vent the products and species produced by the combustion of HTPB and oxygen. The fuel grain holder and burner support are in an enclosure with an exhaust dome above the enclosure to capture the combustion products. An exhaust damper is used to control the flow of air during testing and ducts are used to connect the exhaust fan to the exhaust damper.

Figure 3.17: Exhaust dome used to capture exhaust products during testing.

3.2 GOx and HTPB Methodology

The system described in the previous section uses gaseous oxygen as the main oxidizer, carbon dioxide for the purge system, and methane for the ignition system. Figure displays the full system and fuel grain holder assembly secured within an acrylic box.

The regression rate was calculated from the change in mass of the HTPB fuel grain. The initial and final mass of the fuel was measured for eight tests. The regression rate will be determined by the time averaged change in radius (Equation 3.4) while the average mass flux will use the oxidizer mass flow rate and the initial and final diameter (Equation 3.5).

$$\bar{r} = \frac{D_i - D_f}{2t_b} \tag{3.4}$$

$$G_{ox} = \frac{16\dot{m}_{ox}}{\pi\left(D_i + D_f\right)^2} \tag{3.5}$$

Table3.1 shows the mass flow rate range, between 0.24 – 1.04 g/s, each trial having a 10 second test duration. The regression rate of the fuel grain is then determined by calculating the spatially

averaged change in hole diameter by using Equations 3.1-3.3 to relate the volume change to the change in radius.

$$\pi\left(r_f^2\right)L - \pi(r_i^2)L = \Delta V = \frac{m_i - m_f}{\rho} \tag{3.1}$$

$$\left(r_f^2\right) - (r_i^2) = \frac{\Delta V}{L\pi} \tag{3.2}$$

$$r_f = \sqrt{\frac{\Delta V}{L\pi} + (r_i^2)} \tag{3.3}$$

The regression rate will be determined by the time averaged change in radius (Equation 3.4) while the average mass flux will use the oxidizer mass flow rate and the initial and final diameter (Equation 3.5).

$$\bar{r} = \frac{D_i - D_f}{2t_b} \tag{3.4}$$

$$G_{ox} = \frac{16\dot{m}_{ox}}{\pi\left(D_i + D_f\right)^2} \tag{3.5}$$

Table 3.1: HTPB and Oxygen Hot-Fire Test Matrix

Motor #	Volumetric Flowrate (SLPM)	Initial Burn Time (s)	Secondary Burn Time (s)
1	10±0.5	10±0.1	-
2	15±0.5	10±0.1	-
3	20±0.5	10±0.1	-
4	30±0.5	10±0.1	20±0.1
5	30±0.5	10±0.1	20±0.1
6	30±0.5	10±0.1	20±0.1
7	48±0.5	10±0.1	20±0.1
8	48±0.5	10±0.1	20±0.1

3.3 HAN AND HTPB METHODOLOGY

The system described in Section 3.1 contains gaseous oxygen, nitrogen, and steam as the main oxidizers, and methane for the ignition system. Figure3.4 displays the full system with the added steam generator, heated coils, and nitrogen feed line.

The regression rate model is obtained using the previously mentioned regression rate experiments, measured from six trials. Total mass flowrates for these tests range between 0.64 g/s and 1.04 g/s. Table outlines the different flowrates that were tested for each oxidizer. The

regression rate of the fuel grain is determined by calculating the spatially averaged change in diameter by using Equations 3.1-3.3 to relate the volume change to the change in radius.

Table 3.2: HAN Decomposition and HTPB Hot-Fire Test Matrix

Motor #	Flowrate (SLPM)			Burn Time (s)
	Nitrogen	Oxygen	Syringe Pump	
Check Out Test - 1	9±0.5	9±0.35	0.0±0.005	10±0.05
Check Out Test – 2	9±0.5	9±0.35	0.005±0.005	10±0.05
Check Out Test - 3	9±0.5	9±0.35	0.010±0.005	10±0.05
Check Out Test – 4	9±0.5	9±0.35	0.015±0.005	10±0.05
1	9.6±0.5	9.3±0.35	0.016±0.005	10±0.05
2	9.6±0.5	9.3±0.35	0.016±0.005	10±0.05
3	9.6±0.5	9.3±0.35	0.016±0.005	10±0.05
4	12.8 ±0.5	12.4 ±0.35	0.022 ±0.005	10±0.05
5	12.8 ±0.5	12.4 ±0.35	0.022 ±0.005	10±0.05
6	12.8 ±0.5	12.4 ±0.35	0.022 ±0.005	10±0.05

Chapter 4: Results and Analysis

This chapter presents the results from the gaseous oxygen and HAN decomposition with HTPB testing.

4.1 GOx/HTPB Hot-Fire Results

4.1.1 Regression Rate

The regression rate was calculated using the motor's change in mass, Equations 3.1-3.5. The change in mass was used to calculate the final port diameter of the fuel grain under the assumption that the fuel regression is uniform throughout the port length. Figure 4.1 shows the time average regression rate obtained for oxidizer mass flux ranging from 0.25 to 0.63 g/cm2-s. In Figure 4.1 the dotted line represents the expected regression rate based on DeLuca, et al's baseline model, presented by Equation 3.1 [7].

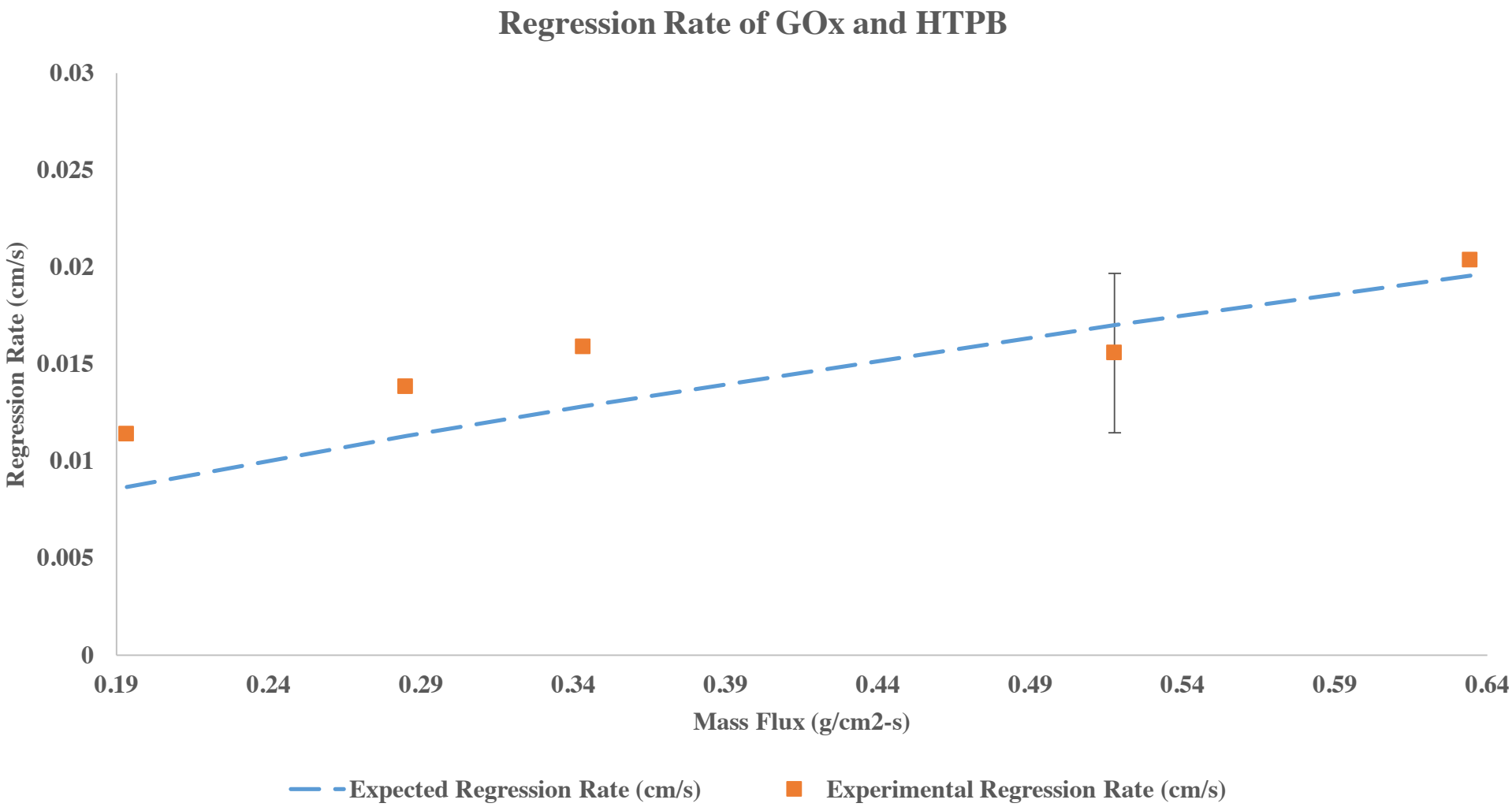

Figure 4.1: Experimental regression rate obtained for mass flux of 0.25 – 0.63 g/cm^2-s.

The results presented in Figure 4.1 show that the experimental data and the expected data agree for the tested mass flux. It should be noted that the baseline model is applicable for flowrates between 8-28 g/cm^2-s, but can be applied outside the limited range. Therefore, the test rig is valid for mass fluxes between 0.25 – 0.63 g/cm^2-s.

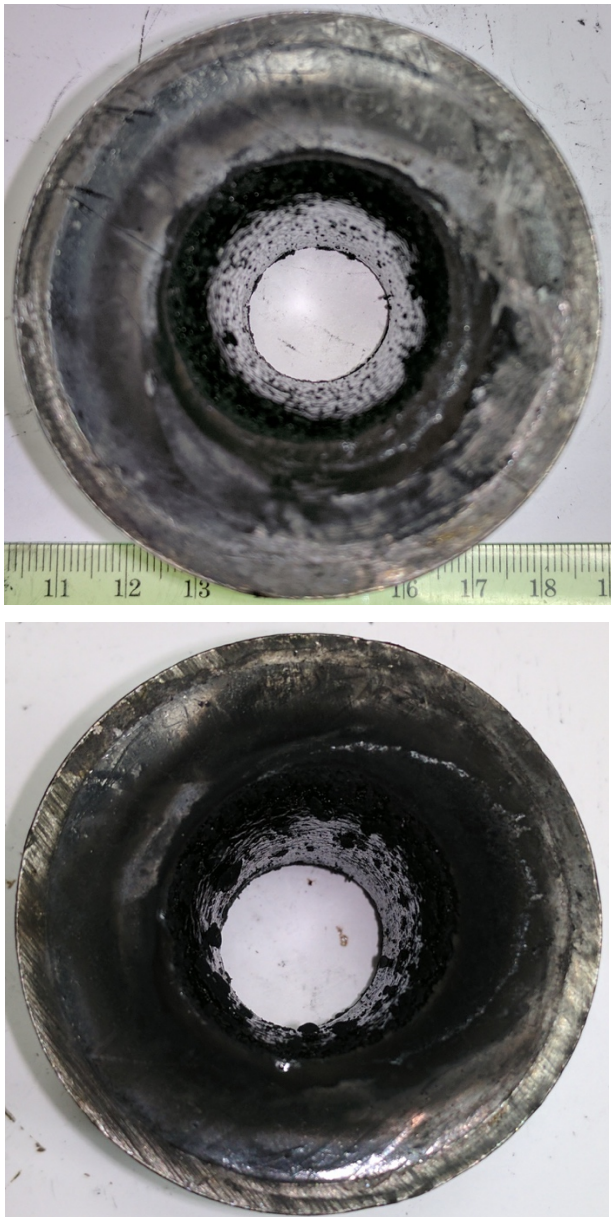

(a) (b)

Figure 4.2: Motor 8 inlet after (a) the initial 10 second burn and (b) secondary 20 second burn.

Figure 4.2 illustrates the motor ports after the initial 10 second burn and 20 second burn for a flowrate of 1.05 g/s. As expected, the final diameter of the motor increased as the flowrate increased and the fuel regression is relatively uniform through the port. Figure4.3 displays the motor outlet for the 10 and 20 second burns for a mass flowrate of 0.64 g/s. After the initial 10 second burn, the outer rim of the outlet displayed a thin charred ring and voids where bubbles formed during the burning. However, the charred ring expanded and covered the entire outlet surface after the 20 second burn. Figure 4.4 displays the motor's port after a 20 second burn and shows the fuel's charred burning patterned.

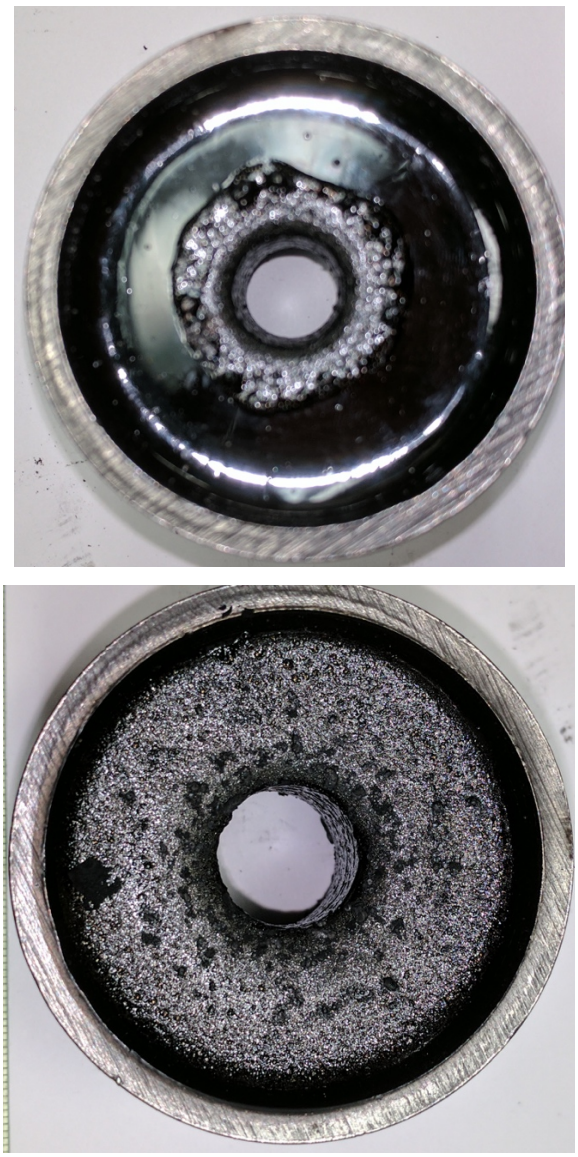

(a) (b)

Figure 4.3: Motor 6 outlet for (a) initial 10 second burn and (b) secondary 20 second burn.

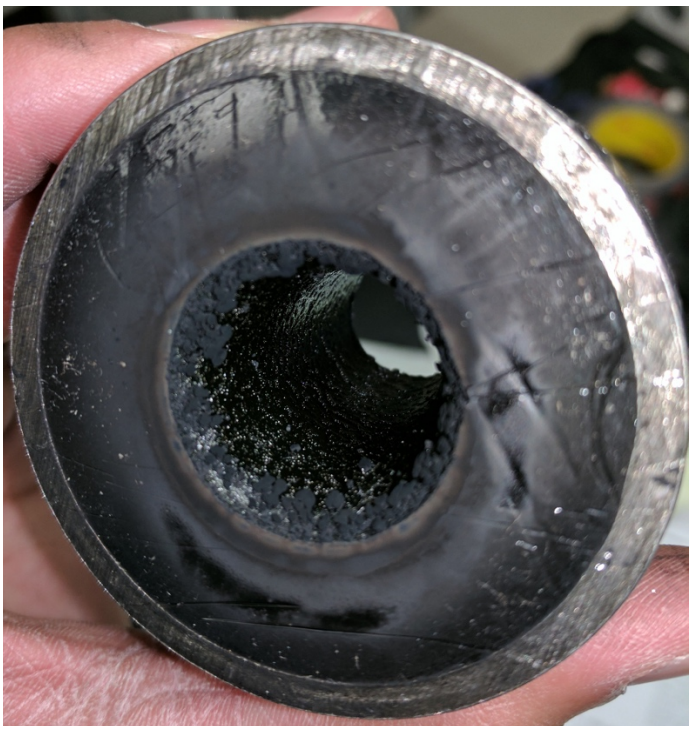

Figure 4.4: Motor 6 port after 20 second burn

4.1.2 Specific Impulse

The specific impulse was determined for each motor by calculating the exhaust velocity, with specific impulse defined as:

$$I_{sp} = \frac{u_e}{g_0} = \frac{\sqrt{\frac{2\gamma RT_c}{\gamma - 1}\left[1 - \left(\frac{p_2}{p_1}\right)^{\frac{\gamma-1}{\gamma}}\right]}}{g_0} \tag{4.1}$$

where γ is the specific heat ratio, R is the specific gas constant, T_c is the combustion temperature, and p_1 is the chamber pressure. The fuel and oxidizer mass flowrates were used to calculate the oxidizer to fuel ratio for each test and each ratio, along with the chamber pressure, were implemented in CEA to determine the specific heat ratio and combustion temperature. Figure 4.5 displays the estimated specific impulses for the hot-fire tests and shows the optimum mixture ratio is around 1.7 with a specific impulse of 114.0 seconds.

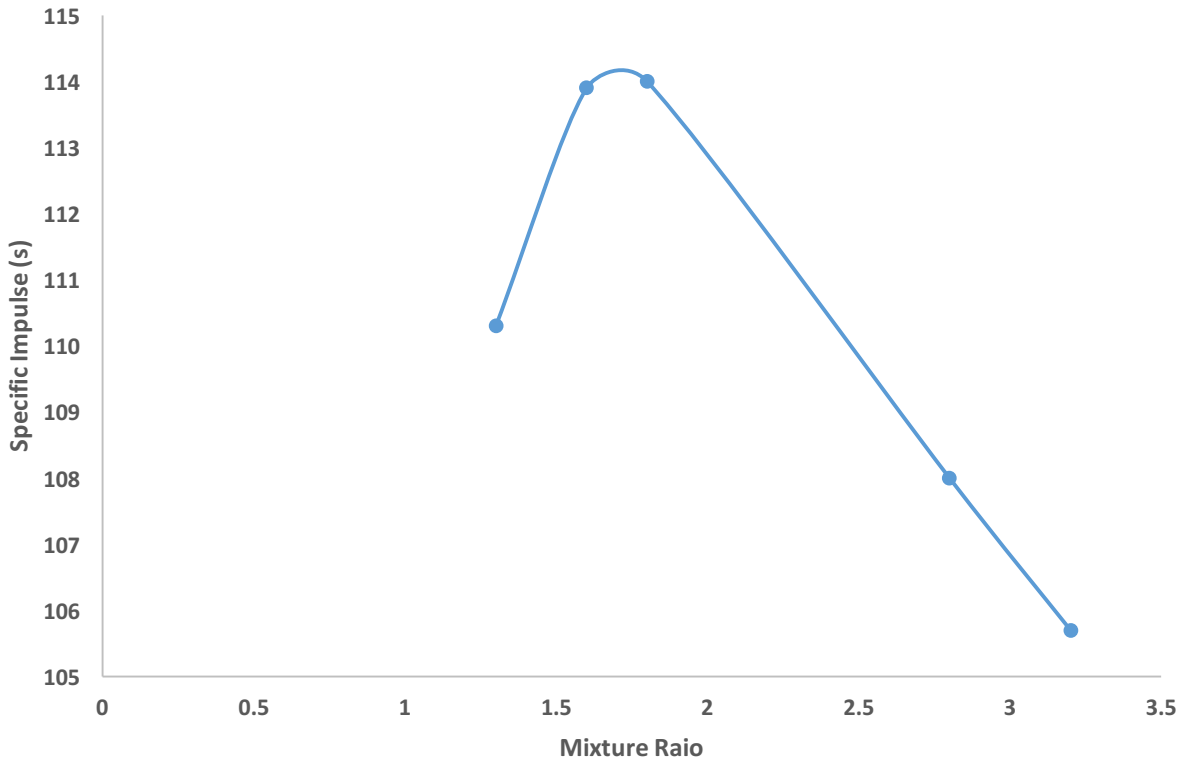

Figure 4.5: Specific impulse estimates for the oxygen and HTPB hot-fire tests.

4.2 REGRESSION RATE OF HAN/HTPB

4.2.1 Regression Rate

The HAN and HTPB testing proved to be difficult. The CEA analysis for HAN decomposition, Table 2.1, showed that steam is a major decomposition species, which was the main obstacle for these tests. For these tests, steam was introduced first and then methane. The handheld igniter was used to light the methane and steam mixture, shown in Figure 4.5. Once oxygen and nitrogen were introduced, the two oxidizers mixed and ignited with the methane briefly before being extinguished.

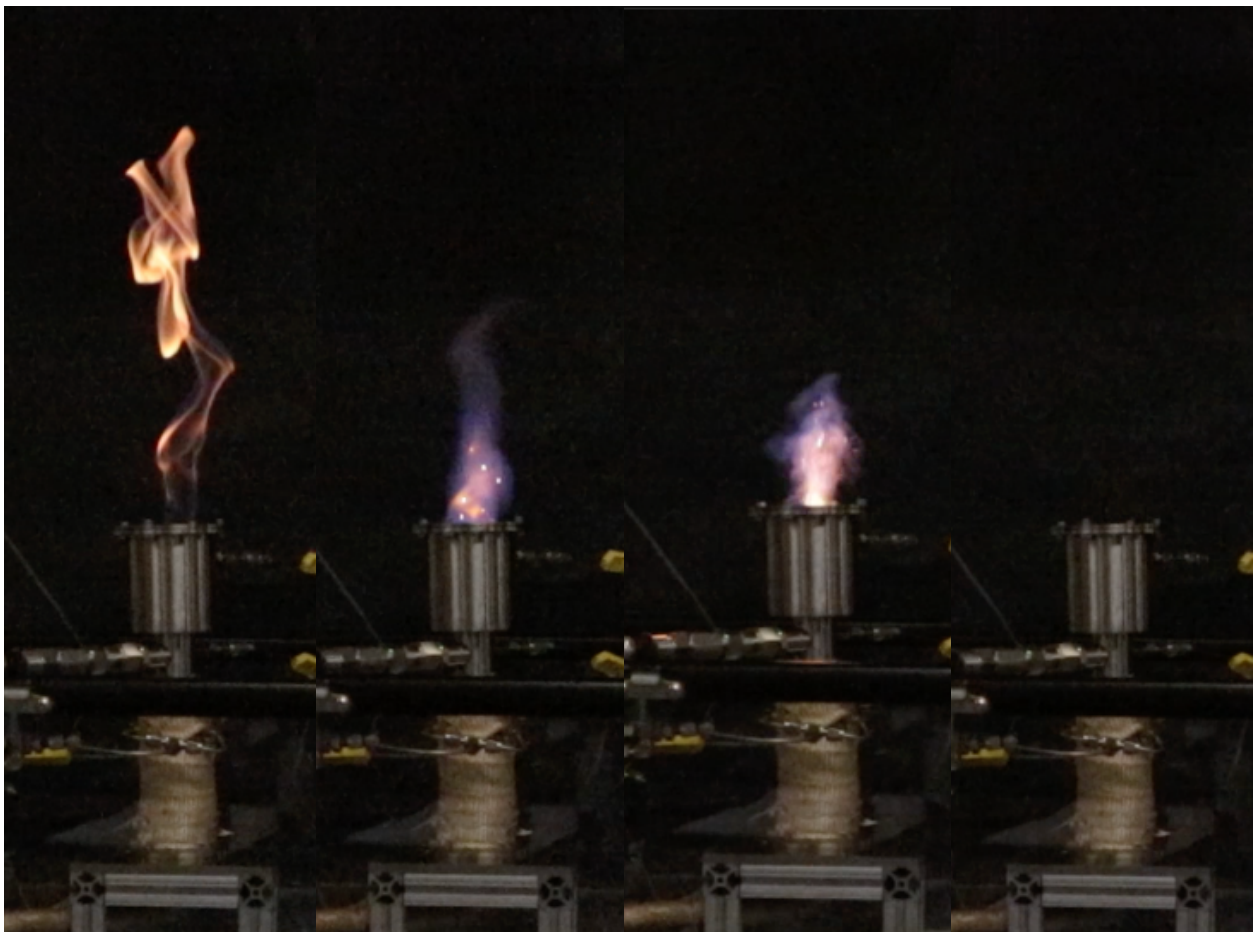

(a) (b) (c) (d)

Figure 4.6: (a) The methane diffusion flame followed by (b, c) an ignition between the oxidizers and methane ending with (d) an extinguished motor.

An expendable fuel grain was used for the check-out tests, where each test slowly increased the amount of steam being introduced. Figure 4.5 details the test run for 9 SLPM of nitrogen and oxygen and 5 mLPM of steam. The difficulties igniting the motor arose from the steam condensing on the fuel grain inlet surface and along the combustion port, preventing the fuel surface from heating up along with extinguishing the oxygen and methane pilot flame. Steam flowrates ranging between 0-5 mLPM were tested to find the maximum amount of steam allowed to enable combustion of the fuel grain. However, the same issue arose with every flowrate aside from 0 mLPM.

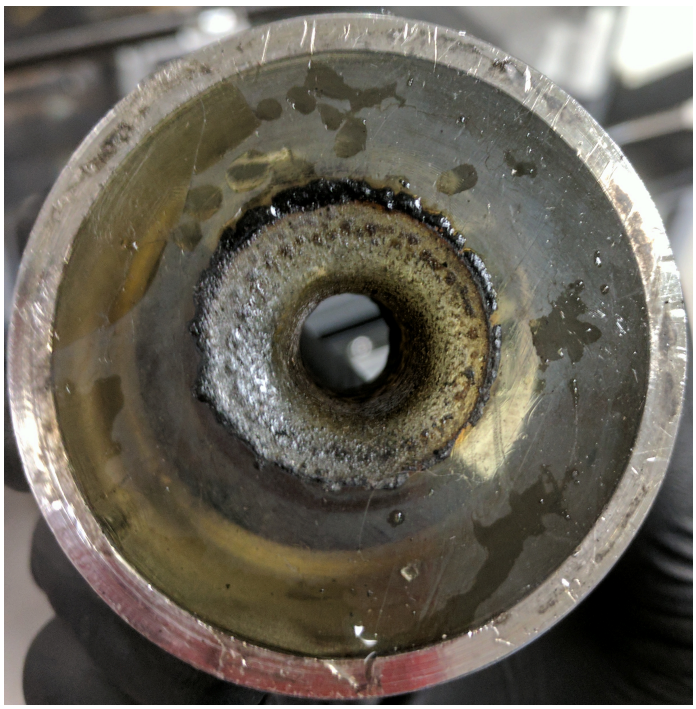

Figure 4.7: Surface of the fuel grain inlet displaying the condensed water gathered from testing.

The adiabatic flame temperature, or the maximum temperature the combustion products can attain without transfer of heat, was calculated for the methane and oxygen pilot flame with varying concentrations of nitrogen and steam. Figure 4.7 shows that the adiabatic flame temperature decreases as the nitrogen concentration increases and while the steam concentration increases. However, the flame temperature is still hot enough to heat up the surface of the HTPB fuel grain to its ignition temperature.

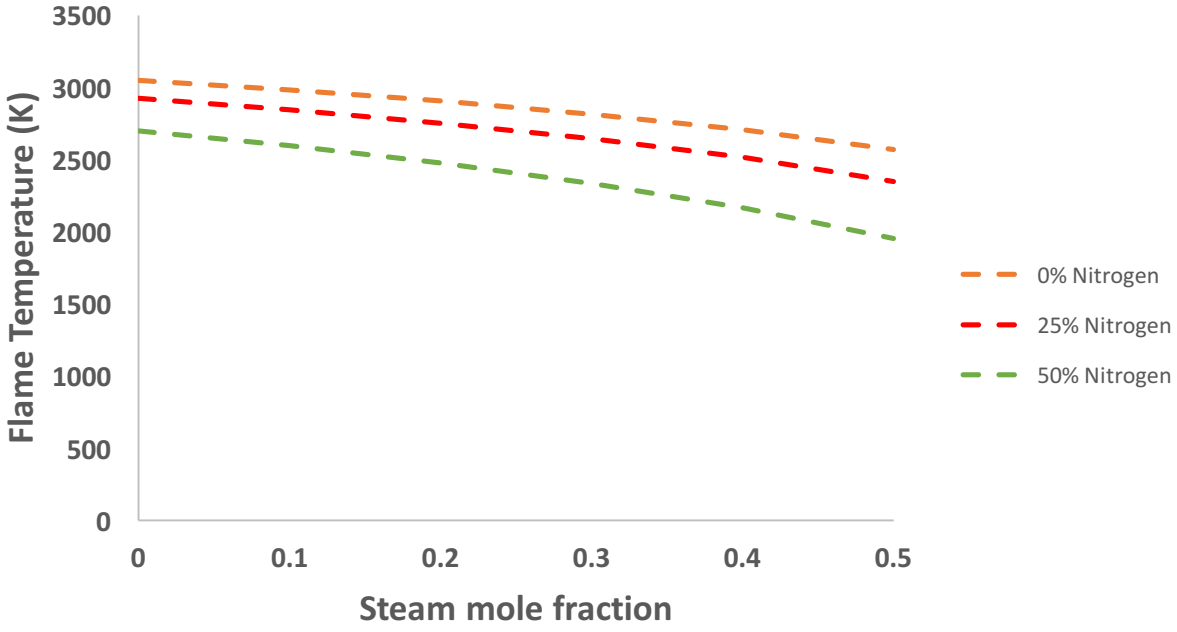

Figure 4.8: Adiabatic flame temperature for the methane and oxygen pilot flame with increasing nitrogen concentration ranged over an increasing steam concentration.

In addition, the motor's small scale exacerbated the difficulties encountered during testing. The steam condensing in the combustion port provided limited surface area for combustion of HTPB and oxygen on this scale. In addition, the large inlet surface area collected condensation throughout each check-out test, shown in Figure 4.6. Testing at a larger scale, for example a larger port diameter, can improve the chances of the HAN decomposition gases igniting with HTPB because it can limit the inlet surface area available for the steam to condense on.

4.2.1 Specific Impulse

The final objective of the project was to estimate the specific impulse for a hybrid propulsion system using AF-M315E and HAN. The specific impulse for 95 wt% HAN solutions have been reported to be 251.1 seconds (Table 1.3). However, there are no publications for specific impulse estimations or measurements for AF-M315E or hybrids employing decomposed HAN.

NASA CEA was used to obtain the specific heat ratio and characteristic velocity for AF-M315E and HTPB for various mixture ratios. Equation 1.1 was then used to calculate the specific impulse, with the thrust coefficient C_F defined as:

$$C_F = \sqrt{\frac{2\gamma^2}{\gamma-1}\left(\frac{2}{\gamma+1}\right)^{\frac{\gamma+1}{\gamma-1}}\left[1-\left(\frac{p_2}{p_1}\right)^{\frac{\gamma-1}{\gamma}}\right]} + \frac{p_e - p_a}{p_c}\left(\frac{A_e}{A^*}\right) \tag{4.2}$$

Figure 4.9 illustrates the predicted specific impulse for AF-M315E employed in a hybrid propulsion system for a chamber pressure of 25 psi where the maximum potential specific impulse is 182.3 seconds.

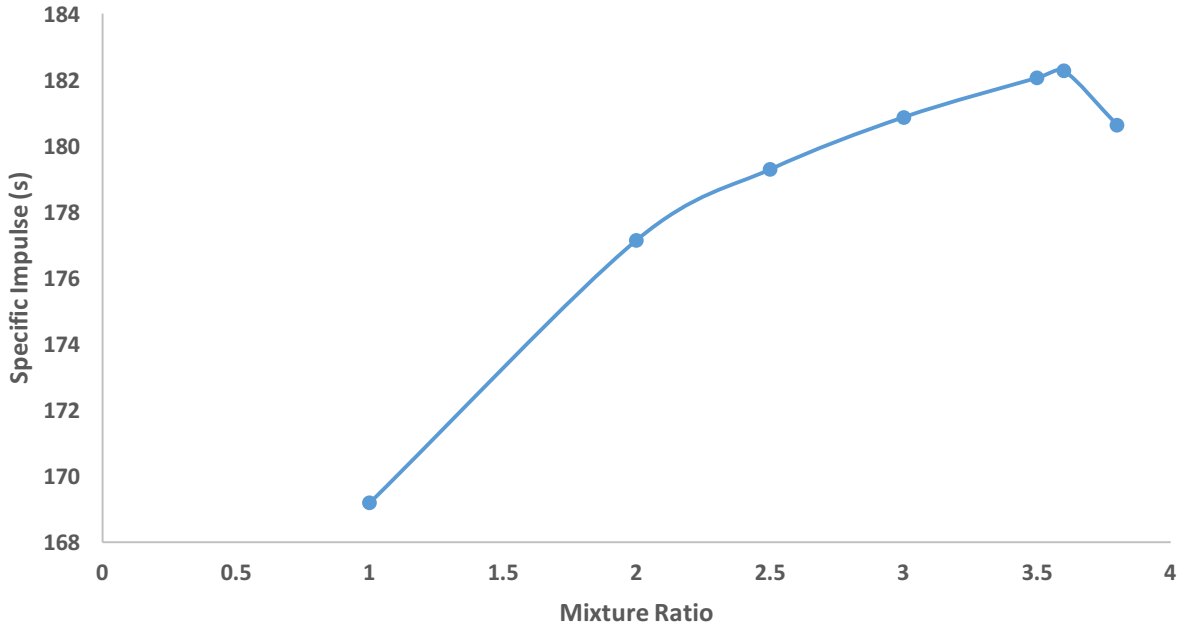

Figure 4.9: CEA predictions of specific impulse for AF-M315E, P_c = 25 psia.

However, Figure 4.9 estimates the specific impulse for a hybrid motor employing liquid AF-M315E rather than the decomposition gases of AF-M315E. Therefore, the same process was used to estimate the specific impulse for hybrids that decompose AF-M315E prior to being injected into the combustion chamber, at three different preheat temperatures: the propellants theoretical decomposition temperature of 1880°C, lower temperature limit of 900°C, and an upper limit of 2000°C. Figure 4.10 shows the estimated specific impulse increases as the preheat temperature increases with a maximum specific

impulse of 184.7 seconds at a mixture ratio of 3.5 occurring if the gases were preheated to 2000°C.

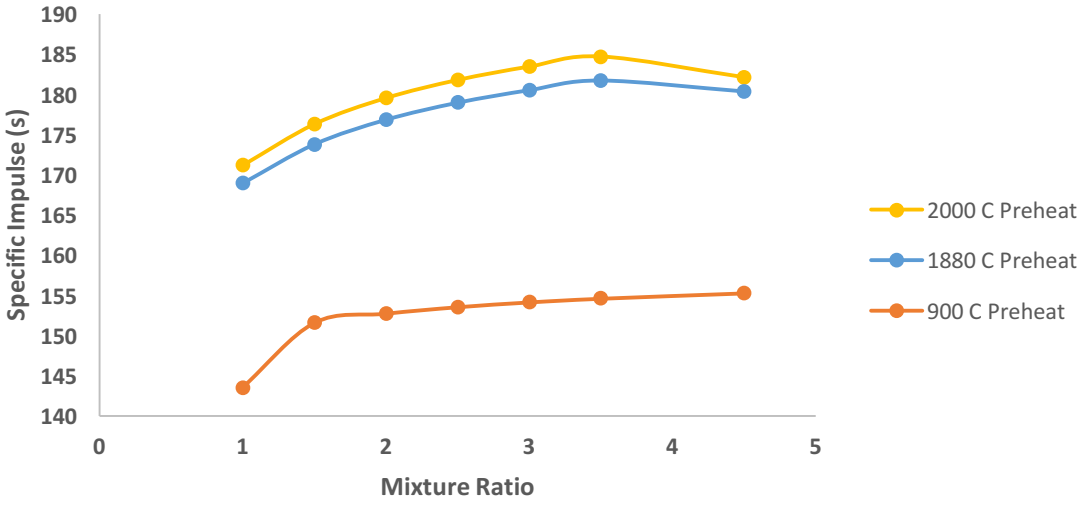

Figure 4.10: CEA predictions of specific impulse for AFM-315E decomposition gases, P_c = 25 psia.

In addition to AF-M315E, the specific impulse for HAN decomposition products and HTPB hybrid motor was estimated at three different preheat temperatures: the propellants theoretical decomposition temperature of 900°C, decomposition temperature reported in literature of 180°C, and an upper limit of 2000°C. Figure 4.11 illustrates the specific impulse increasing as the preheat temperature increases, with a max specific impulse of 279.2 seconds at a mixture ratio of 7. Comparing the three options, the HAN decomposition products offer higher performance mainly due to the higher concentration of oxygen. The specific impulse for HAN decomposition products preheated at 180°C is even higher than the specific impulse for AF-M315E decomposition products preheated at 2000°C.

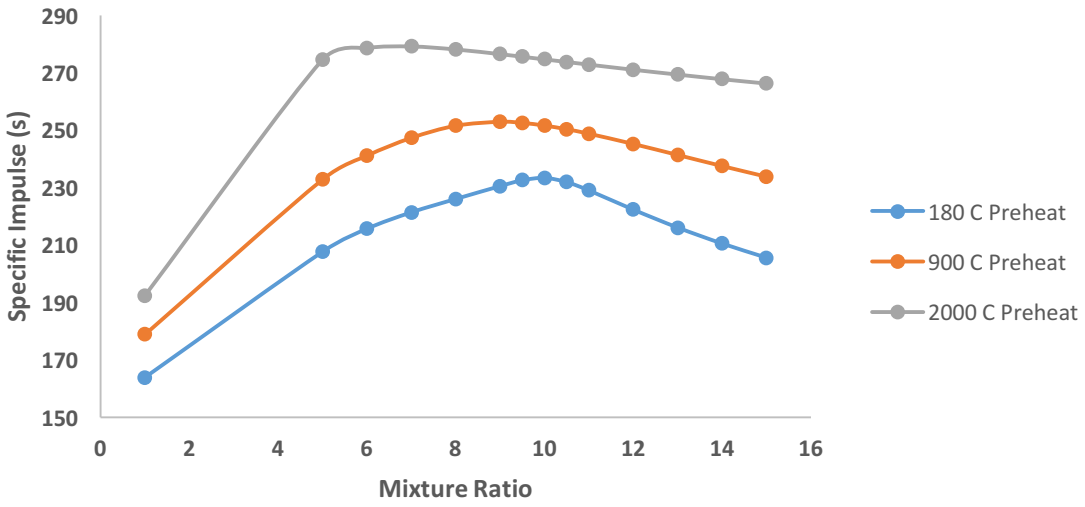

Figure 4.11: CEA predictions of specific impulse for HAN decomposition gases, P_c = 25 psia.

Chapter 5: Conclusion

5.1 SUMMARY

The research team was tasked with measuring the regression rate of HAN decomposition products and HTPB and estimating the specific impulse of hybrid propulsion systems using AF-M315E and HAN decomposition products.

In summary, this study presents the following:

- Design and development of a small-scale test stand to test and measure the regression rate of gaseous oxygen and the HAN decomposition products with HTPB
- Validation of the test stand from by comparing the experimental regression rate of oxygen and HTPB with empirical models found through literature. The experimental regression rate ranged between 0.011 – 0.20 cm/s and shown a good correlation with DeLuca, et al's model [7], with the error between the experimental and predicted regression rate being within 20%.
- Estimation of specific impulse for the oxygen and HTPB hot-fire test along with hybrid systems employing AF-M315E and HAN decomposition products. For the hot-fire test, the maximum I_{sp} was 114.0 seconds at a mixture ratio of 1.8. The specific impulse using HAN decomposition products was estimated to be 252.5 seconds, much higher than the 181.7 seconds estimated for AF-M315E decomposition products.
- Investigation of the applicability of HAN decomposition products in a hybrid propulsion system. The HAN testing showed the difficulties of igniting the hybrid rocket because of the high concentration of steam from the decomposition process. The steam proved to be an obstacle as it condensed on the surface of the fuel grain inlet and along the port.

5.2 FUTURE WORK

This study focused on validation of the test stand and measuring the regression rate of HTPB and HAN decomposition products obtained from CEA. Future work includes:

- Testing the HAN decomposition products with HTPB fuel grains with larger port diameters.
- Measuring regression rate of HAN and AF-M315E decomposition products obtained experimentally
- Studying the regression rate using the multipurpose optically accessible combustor (MOAC) and solid fuel grain slab by investigating the effects of chamber pressure, oxidizer mass flux, and coaxial shear injector characteristics on the regression rate. This task using the coaxial shear injector will provide a baseline regression rate model.
- Studying the effect the coaxial swirl injector on the regression rate and chamber mixing. This task will integrate the coaxial swirl injector into the MOAC to enhance turbulent mixing and potentially reduce the characteristic length. Different injector geometries will be tested such as different orifice port diameters, port numbers, and impingement angles.

References

[1] Altman, D., and Holzman, A. 2007. “Overview and Hisotry of Hybrid Rocket Propulsion,” *Fundamentals of Hybrid Rocket Combustion and Propulsion*, Progress in Astronautics and Aeronautics, edited by M. Chiavernini and K. K. Kuo, Vol. 218, AIAA, Reston, VA.

[2] Biddle, R.A., and Sutton, E.S., "Highly Soluble, Non-Hazardous Hydroxylammonium Salt Solutions for use in Hybrid Rocket Motors," U.S. Patent 4,527,389, 9 July 1985.

[3] Brown, C. D. 1996. Spacecraft Propulsion. Washington, DC: American Institute of Aeronautics and Astronautics, Inc.

[4] Cantwell, B. 2007. "Hybrid Rockets," Personal Collection of Cantwell, Standford University, Stanford, California.

[5] Corthéoux, L., Amariei, D., Rossignol, S., Kappenstein, C. 2006. “Thermal and Catalytic Decomposition of HNF and HAN liquid ionic as propellants”, *Applied Catalysis B: Environmental*. Volume 62. Elsevier.

[6] Corthéoux, L. et al. 2004. “Thermal and Catalytic Decomposition of HNF and HAN-based propellants”, *Proceedings of the 2nd International Conference on Green Propellants for Space Propulsion*, Sardina, Italy.

[7] Deluca, L., Galfetti, L., Colombo, G., Maggi, F., Bandera, A., Boiocchi, M., . . . Reina, A. (2011). Time-resolved burning of solid fuels for hybrid rocket propulsion. *Progress in Propulsion Physics*.

[8] Heister, H., and Wernimont, E. 2007. "Hydrogen Peroxide, Hydroxyl Ammonium Nitrate, and Other Storable Oxidizers,"*Fundamentals of Hybrid Rocket Combustion and Propulsion*, Progress in Astronautics and Aeronautics, edited by M. Chiavernini and K. K. Kuo, Vol. 218, AIAA, Reston, VA.

[9] Karabeyoglu, A. 2007. "Combustion Instability and Transient Behavior in Hybrid Rocket Motors," *Fundamentals of Hybrid Rocket Combustion and Propulsion*, Progress in Astronautics and Aeronautics, edited by M. Chiavernini and K. K. Kuo, Vol. 218, AIAA, Reston, VA.

[10] Kuo, K. K., and Chiaverini, M. 2007. “Challenges of Hybrid Rocket Propulsion in the 21st Century,” *Fundamentals of Hybrid Rocket Combustion and Propulsion*, Progress in Astronautics and Aeronautics, edited by M. Chiavernini and K. K. Kuo, Vol. 218, AIAA, Reston, VA.

[11] Lee, H., and Litzinger, T. A. 2001. “Thermal Decomposition of HAN-based Liquid Propellants”, *Combustion and Flame*, Vol. 127. Elsevier.

[12] Lee, H., and Litzinger, T. A. 2003. "Chemical Kinetic Study of HAN Decomposition", *Combustion and Flame,* Vol. 135. Elsevier.

[13] Marxman, G. A., and Gilbert, M., “Turbulent Boundary Layer Combustion in the Hybrid Rocket,” *Ninth International Symposium on Combustion*, Academic Press, New York, 1963.

[14] Marxman, G., R. Muzzy, and C. Wooldridge. "Fundamentals of hybrid boundary layer combustion." *Heterogeneous Combustion Conference*, 1963. doi:10.2514/6.1963-505.

[15] Newlands, R. 2009. Introduction to Hybrid Design. Boston University: Boston, MS.

[16] Rice, E., Gustafson, R., Chiaverini, M., Clair, C. S., & Knuth, W. (2000). Mars ISRU CO/O2 hybrid engine development status. *38th Aerospace Sciences Meeting and Exhibit*.

[17] Smoot, L. D. and Price, C. F., "Pressure Dependence of Hybrid Fuel Regression Rates," AIAA Journal, Vol. 5, No. 1, 1967. pp. 102-106.

[18] Sutton, G. P., and Biblarz, O. 2001. Rocket Propulsion Elements. 7th ed. John Wiley & Sons: New York, NY.

[19] "UNITED STATES DEPARTMENT OF LABOR." Chemical Sampling Information | Hydrazine | Occupational Safety and Health Administration. Accessed December 25, 2016. https://www.osha.gov/dts/chemicalsampling/data/CH_245900.html.

[20] Zilliac, Gregory, and M. Karabeyoglu. "Hybrid Rocket Fuel Regression Rate Data and Modeling."*42nd AIAA/ASME/SAE/ASEE Joint Propulsion Conference and Exhibit*, 2006. doi:10.2514/6.2006-4504.

Appendix A: HAN Decomposition CEA Analysis

```
*************************************************************************
*******

      NASA-GLENN CHEMICAL EQUILIBRIUM PROGRAM CEA2, MAY 21, 2004
            BY  BONNIE MCBRIDE AND SANFORD GORDON
     REFS: NASA RP-1311, PART I, 1994 AND NASA RP-1311, PART II, 1996

*************************************************************************
*******



 problem
    hp   p,psia=14.7,  t,c=180
 react
  oxid=HAN wt=0.95
  oxid=H2O(L) wt=0.05  t,c=22
 output  massf
 end

 OPTIONS: TP=F  HP=T  SP=F  TV=F  UV=F  SV=F  DETN=F  SHOCK=F  REFL=F
INCD=F
 RKT=F  FROZ=F  EQL=F  IONS=F  SIUNIT=T  DEBUGF=F  SHKDBG=F
DETDBG=F  TRNSPT=F

 T,K =   453.1500

 TRACE= 0.00E+00  S/R= 0.000000E+00  H/R= 0.000000E+00  U/R= 0.000000E+00

 P,BAR =     1.013525

   REACTANT         WT.FRAC   (ENERGY/R),K   TEMP,K  DENSITY
      EXPLODED FORMULA
 : HAN             0.950000  -0.530179E+04   298.15  0.0000
       H  4.00000  N  2.00000  O  4.00000
 : H2O(L)          0.050000  -0.344044E+05   295.15  0.0000
       H  2.00000  O  1.00000

 SPECIES BEING CONSIDERED IN THIS SYSTEM
(CONDENSED PHASE MAY HAVE NAME LISTED SEVERAL TIMES)
 LAST thermo.inp UPDATE:    6/04/15
```

```
 g 6/97  *H            g10/01  HNO           tpis89  HNO2
 g 5/99  HNO3            g 4/02  HO2           tpis78  *H2
 g 8/89  H2O           g 6/99  H2O2          g 5/97  *N
 g 4/99  *NH           g 3/01  NH2           tpis89  NH3
 tpis89  NH2OH           tpis89  *NO            g 4/99  NO2
 j12/64  NO3           tpis78  *N2            g 5/99  N2H2
 tpis89  NH2NO2          g 4/99  N2H4            g 4/99  N2O
 g 4/99  N2O3          tpis89  N2O4          g 4/99  N2O5
 tpis89  N3            g 4/99  N3H           g 5/97  *O
 g 4/02  *OH           tpis89  *O2           g 8/01  O3
 g11/99  H2O(cr)         g 8/01  H2O(L)          g 8/01  H2O(L)

O/F =   0.000000

                EFFECTIVE FUEL     EFFECTIVE OXIDANT       MIXTURE
ENTHALPY              h(2)/R           h(1)/R            h0/R
(KG-MOL)(K)/KG      -0.14792914E+03    -0.14792914E+03    -0.14792914E+03

KG-FORM.WT./KG          bi(2)            bi(1)            b0i
 *H              0.45116554E-01    0.45116554E-01    0.45116554E-01
 *N              0.19782855E-01    0.19782855E-01    0.19782855E-01
 *O              0.42341132E-01    0.42341132E-01    0.42341132E-01

POINT ITN      T          H          N          O
  1   13    2499.197    -12.630    -14.601    -15.553



      THERMODYNAMIC EQUILIBRIUM COMBUSTION PROPERTIES AT
ASSIGNED

                    PRESSURES

CASE =

        REACTANT              WT FRACTION      ENERGY      TEMP
                           (SEE NOTE)     KJ/KG-MOL      K
        HAN                  0.9500000    -44081.800    298.150
        H2O(L)               0.0500000   -286056.128    295.150

 O/F=    0.00000  %FUEL=100.000000  R,EQ.RATIO= 0.532775  PHI,EQ.RATIO=
0.000000

 THERMODYNAMIC PROPERTIES
```

P, BAR 1.0135
T, K 2499.20
RHO, KG/CU M 1.1325-1
H, KJ/KG -1229.96
U, KJ/KG -2124.88
G, KJ/KG -31527.3
S, KJ/(KG)(K) 12.1228

M, (1/n) 23.219
(dLV/dLP)t -1.00648
(dLV/dLT)p 1.1698
Cp, KJ/(KG)(K) 3.6861
GAMMAs 1.1448
SON VEL,M/SEC 1012.2

MASS FRACTIONS

*H 0.00009
HO2 0.00005
*H2 0.00055
H2O 0.38688
*NO 0.01599
NO2 0.00002
*N2 0.26962
*O 0.00458
*OH 0.02611
*O2 0.29612

* THERMODYNAMIC PROPERTIES FITTED TO 20000.K

PRODUCTS WHICH WERE CONSIDERED BUT WHOSE MASS FRACTIONS WERE LESS THAN 5.000000E-06 FOR ALL ASSIGNED CONDITIONS

HNO HNO2 HNO3 H2O2 *N
*NH NH2 NH3 NH2OH NO3
N2H2 NH2NO2 N2H4 N2O N2O3
N2O4 N2O5 N3 N3H O3
H2O(cr) H2O(L)

NOTE. WEIGHT FRACTION OF FUEL IN TOTAL FUELS AND OF OXIDANT IN TOTAL OXIDANTS

Appendix B: Burner Support Drawing

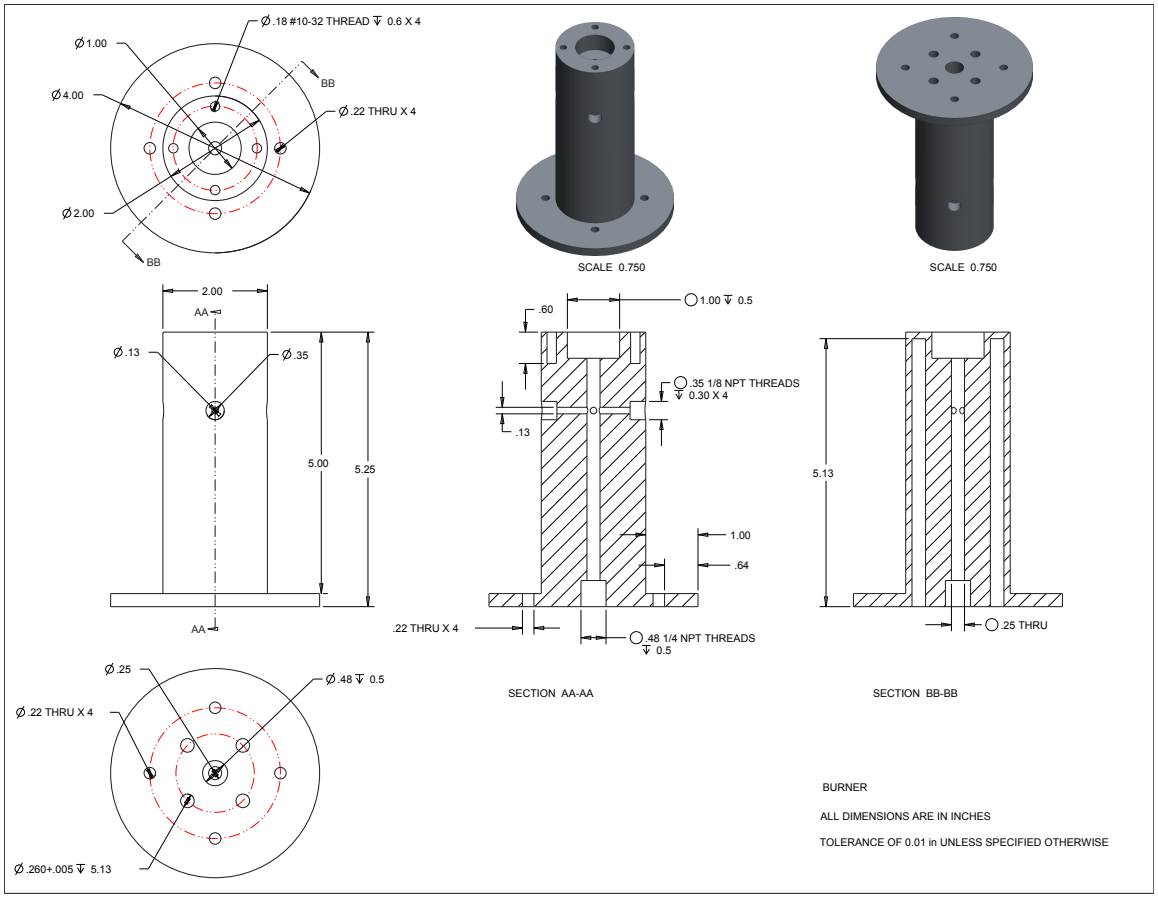

Appendix C: HTPB Mixing Procedure

INTRODUCTION

SCOPE

The AF-M315E decomposition system is designed to decompose AF-M315E, an Air Force Developed propellant, and measure the chemical makeup and concentrations of the propellant's decomposition gases. The propellant reacts with a preheated iridium coated silicon carbide foam catalyst, contained within an alumina holder. The propellant decomposes into different gases that are then passed through a heat sink to remove some heat from the gases before they are captured in a sample cylinder. After the cylinder has cooled, the gases are then analyzed with a mass spectrometer. The results of these tests will be used to replicate the decomposition gases of AF-M315E and attempt to use them as an oxidizer for a hybrid rocket propulsion system in conjunction with HTPB as the fuel.

The HTPB fuel grain will be housed inside of a combustion chamber where the simulated AF-M315E gases will flow as oxidizer and the fuel grain will be ignited. The goal of this project is to test the combustion properties of HAN-HTPB combination and improve the efficiency and regression rate of HAN-HTPB.

PROCEDURE OBJECTIVES

Fabricate HTPB Test Articles.

- To fabricate the test articles, HTPB will be combined with a curative to create a test article with a homogenous fuel grain.

PROCEDURE LOGISTICS

Procedure Name: HTPB Test Article Fabrication
Procedure Number: _____

Procedure Date: _____

Location:

Engineering Bldg. Room M205
University of Texas at El Paso
500 W. University Ave.
El Paso, TX 79968

Personnel Breakdown and Contact Info:

Role	Name	Phone	Email
Procedure Conductor			
Procedure Operator			
Principle Investigator	Norman Love	(915)747-8981	ndlove@utep.edu
cSETR Safety Manager	Scott Hill	(915)747-8945	cshill2@utep.edu

MATERIALS

Liquid HTPB Binder (R-45HTLO)

WEIGHT (± 1g): 287g

Isophorone Diisocyanate (IPDI)

WEIGHT (± 0.1g): 26g

Carbon Black

WEIGHT (± 0.01g): .783g

Aluminum Foil Roll
Saran Wrap (Approx. 4 sq in)x3
Laboratory Scale (± 0.01g)
Triple Beam Balance (± 1g)
Glass Stirring Rod
Beakers (Glass, 1 Liter)x2
Glass panels (3x3)x2
Steel Pipe Nipples (2″Pipe x 2″L)x3
Rubber bands x6
PF Degreaser
Acetone
Cheese Cloth
Labels x2
Marker

SAFETY HAZARDS

Concern No.	Concern	Initial RAC	Residual RAC	Residual Risk	Mitigating Feature
1	Exposure of personnel to toxic fumes generated by uncured propellant	3C	3E	Low	Mixing procedure will done in a fume hood a motors will be covere with glass panel
2	Asphyxiation due to venting of IPDI, in an enclosed room results in death or injury to personnel	2C	2E	Low	Mixing procedure will done in a fume hood a motors will be covere with glass panel

SAFETY PRECAUTIONS

Use approved personal protective equipment (PPE):

Eyes: Safety goggles shall be worn during the entirety of the mixing process.

Ears: No hearing protection will be necessary for mixing HTPB.

Hands: Latex Protective gloves shall be worn during the entirety of the mixing process.

Clothing: A fire resistant lab coat shall be worn for the entire procedure

All personnel shall wear approved personal protective equipment for the operation being performed as defined below:

General Operations:

Eyes	Safety goggles shall be worn at all times when inside Lab M205
Feet	Closed toe shoes shall be worn at all times when inside Lab M205
Ears	No hearing protection is required in Lab M205

If any personnel injury occurs, the following is offered as a guide:

- Isolate or remove the hazard from the area.
- Move injured personnel only if necessary to prevent further injury.
- Call for medical help.
  - Medical/Ambulance 911
  - Fire Department 911
  - UTEP PD 915-747-5611
  - Environmental Incident 911
  - Medical Center 915-747-5624
  - Safety Hotline 911
  - Dr. Choudhuri 915-747-5611

INITIAL SETUP AND CHECKOUT PROCEDURES

ENSURE FUME HOOD IS FUNCTIONAL

Switch the fume hood power switch to "On" if it is not already in the "On" position
Check that air is being pulled from the fume hood by verifying that the airflow monitor is indicating "safe"
If any of steps 3.1.1 – 3.1.2 do not produce the expected result, abort the procedure and investigate

ENSURE VACUUM CHAMBER IS FUNCTIONAL

Close the vacuum chamber by placing the bell jar portion on top of the chamber base
Open fume hood vacuum valve
Verify vacuum is being pulled on the chamber by physically pulling on the bell jar portion of the chamber. If there is vacuum and a good seal, the bell jar will be held firmly to the base of the chamber by the vacuum.
If any of steps 3.2.1 – 3.2.3 do not produce the expected result, abort the procedure and investigate

ENSURE OVEN IS FUNCTIONAL

Switch the oven power switch to "On"
Set the oven temperature controller to 100°F
Verify that the oven reading attains and maintains 63 ± 5°C for 5 minutes
If any of steps 3.3.1 – 3.3.3 do not produce the expected result, abort the procedure and investigate

TEST PROCEDURES

MOLD FABRICATION

Completely cover one end of the steel pipe with saran wrap, straighten it out carefully and secure it with a rubber band (Figure 1 below)
Place one glass panel underneath one end of the pipe
This pipe/saran wrap/rubber band/glass assembly will be referred to as the "Motor Mold" or "Mold" from this point forward

Figure 1

SAFETY WALK DOWN PRIOR TO MIXING

Notify all personnel around and in M205 of hazardous operations
Ensure M205 is cleared of non-authorized personnel
Secure door access and all entries to Lab M205

INGREDIENTS WEIGH UP

Do not weigh ingredients more than 24 hours prior to mixing phase

For ingredient amounts, refer to 1.4 Materials

Cut out a square of aluminum foil (12″ x 6″) and fold it to roughly 6″ x 6″
Lightly create a "tray" using the aluminum foil to contain carbon black
Using the laboratory scale, weigh the aluminum foil tray and record it as tare weight
Measure out the amount of carbon black using the aluminum foil "tray" and weigh using laboratory scale
Using the triple beam balance, weigh each container (1L beaker) and record these as tare weights
Clearly label each container with labels marked "R-45HTLO" and "IPDI" to avoid confusion during the mixing phase
Measure out the amount of R-45HTLO to be mixed and cover the container with aluminum foil
Measure out the amount of IPDI to be mixed and cover the container with aluminum foil

MIXING

Place R-45HTLO container on the center of the vacuum chamber base

Lock the "Bell Jar" portion of the vacuum chamber onto the base of the chamber, enclosing the R-45HTLO container

Open the vacuum valve on the fume hood to pull a vacuum on the chamber

Watch the container inside the vacuum chamber and note the formation of a foam layer of bubbles as the vacuum increases. (Figure 2)

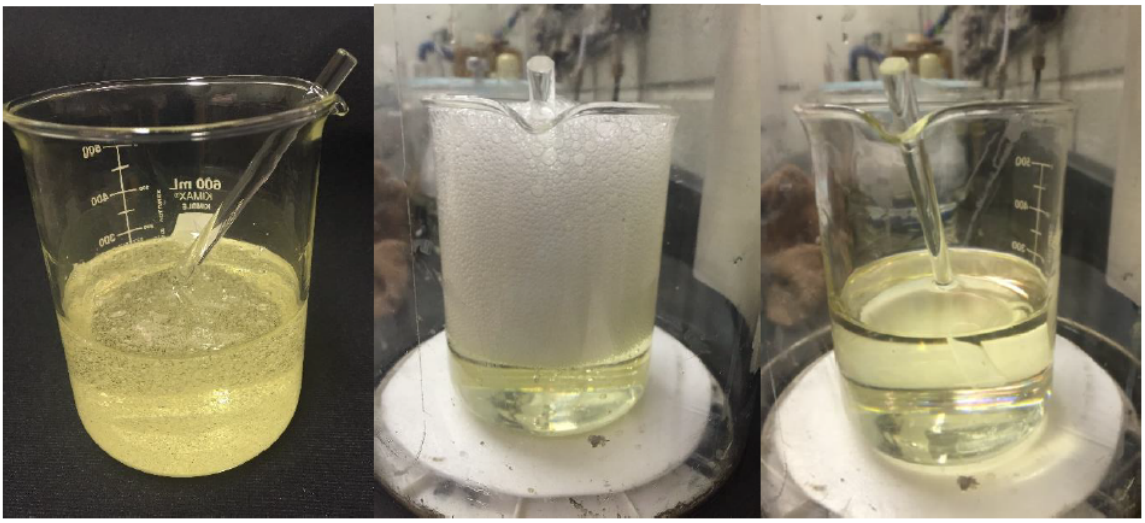

Figure 2: (Left) The R-45 chemical with entrained bubbles. (Middle) The bubbles being vacuumed out of the R-45 chemical. (Right) The R-45 chemical after completing the vacuum cycles and no longer containing bubbles.

When this layer reaches the top of the container, break the vacuum in the chamber to "pop" the bubbles that were formed

Repeat steps 4.4.2 through 4.4.5 until bubbles no longer reach the top of the container. When this occurs proceed to step 4.4.7 (The vacuum procedure will need to be repeated at least 10 – 20 times)

Set the vacuum chamber to its highest setting and leave it until all of the visible bubbles have been removed from the R-45HTLO liquid

Carefully and slowly add the curative, IPDI, to the R-45HTLO liquid to minimize the entrainment of air into the mixture

Carefully unload the carbon black into the two liquids

Mix the two liquids and carbon black thoroughly and slowly for 15 minutes with glass stirrer to minimize air entrained in the mixture

Place R-45HTLO/IPDI container on the center of the vacuum chamber base

Lock the "Bell Jar" portion of the vacuum chamber onto the base of the chamber, enclosing the R-45HTLO/IPDI container

Initiate vacuum cycle until all of the visible bubbles have been removed from the R-45HTLO/IPDI mixture

Remove the mixture from the vacuum chamber

Hold a motor mold and slowly pour the mixture into the mold, being careful not to entrain air into the mixture

Repeat 4.4.14 for the other two motors

Place a motor mold on the center of the vacuum chamber base

Lock the "Bell Jar" portion of the vacuum chamber onto the base of the chamber, enclosing the motor mold

Initiate vacuum cycle until all of the visible bubbles have been removed from the motor mold

Remove the motor from the vacuum chamber

Leave the motor in the fume hood and allow for the motor mold to cure at ambient conditions

Repeat 4.4.16 – 4.4.20 for the other two motors

Clean up the mixing area as outlined in Section 4.5 of this procedure

After 24 Hours minimum

Place a glass panel on the end of a motor facing up (should now have both ends of the SS pipe covered with glass panels)

Place the mold into the oven

Repeat 4.4.23 - 4.4.24 for the other two motors (Skip if doing remedial cycle)

Secure the oven and set the temperature to 63°C ± 5°C and the time to the oven's maximum setting (9999 min)

Every 24 Hours

Check to ensure that the oven is still functioning at 63 ± 5°C. If the motor is on a remedial oven cycle, as described in Step 4.4.35 of this procedure, remove the motor and proceed to step 4.4.34

After 7 Days

Remove the mold from the oven
Use the glass stirrer to press on the fuel grain to ensure that it has fully cured
If the fuel is firm and not runny, proceed to step 4.4.36. If manual test fails, return to step 4.4.29, allowing the motor a remedial oven cycle 18 – 36 hours to cure. If the motor still has not cured after 4 remedial cycles, dispose of the motor through EH&S and investigate why the motor didn't cure
Perform post-processing procedure

CLEAN UP

Wet down components with fuel with PF Degreaser and cheese cloth
Clean each part with PF Degreaser and cheese cloth
Wipe down each component with acetone, this will be performed inside of the fume hood
The soiled cheese cloth will be disposed of via EH&S solid waste removal procedures
Dispose of residual mixture via EH&S solid waste removal procedures

EMERGENCY PROCEDURES

PERSONNEL INJURY

If personnel injury occurs, the following is offered as a guide:

- Isolate or remove hazard from area.
- Move injured personnel only if necessary to prevent further injury.
- Call for medical help.

o Medical/Ambulance	911
o Fire Department	911
o UTEP PD	915-747-5611
o Environmental Incident	911
o Medical Center	915-747-5624
o Safety Hotline	911
o Dr. Choudhuri	915-747-5611

Nomenclature:
Equivalent Weight (EW)
Index Ratio (IR)

EW (R-45HTLO) Calculations

	Associated Value:	EW:
EW (R-45HTLO) by Hydroxyl Number	47.1	1234.6

EW (IPDI) Calculations

	Associated Value:	EW:
EW (IPDI) by %NCO	37.8	111.1111111

Curative Calculations:

	Associated Value:
EW (R-45HTLO) (g/eq) (Manual Input)	1234.6
EW (IPDI) (g/eq)	111.1111111
IR (1.0 is Ideal)	1
Amount of R-45HTLO by Weight (g)	287
Amount of IPDI by Weight (g)	26

Chemical Weights for HTPB Mixture:

R-45HTLO (g ± 1):	IPDI (g ± 0.1):
287	**26**

Appendix D: GOx and HTPB Flame Lengths

In addition to measuring the regression rate, the flame length for each hot-fire test was interpolated using a length scale present in each video. Figure 4.5 illustrates the average flame length observed during testing. The flame length is the distance from the flame zone to the flame tip and aids in determining the combustion chamber characteristic length, L^*. The characteristic length is the minimum length needed for the combustion chamber to attain near-equilibrium combustion.

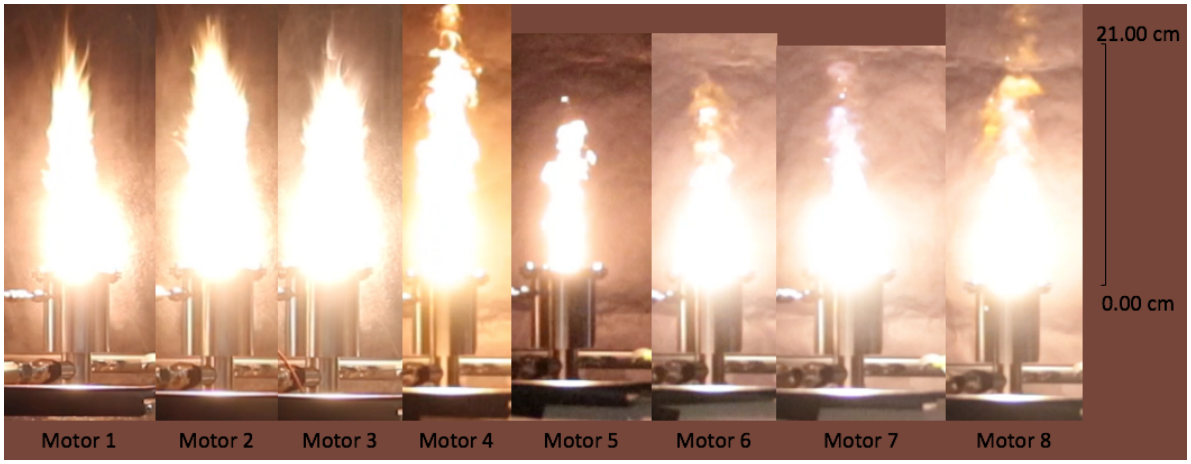

Figure C.1: Average flame length observed for each motor.

Appendix E: Specific Impulse Sample Calculations

Table E.1: Parameters for Liquid Oxygen and HTPB hybrid motor

Parameter	Value
Chamber Pressure, $\boldsymbol{P_c}$ (Pa)	172369
Mixture Ratio	2.3
Specific heat ratio, $\boldsymbol{\gamma}$	1.14
Characteristic velocity, $\boldsymbol{c^*}$ (m/s)	1796.4
Exit Pressure, $\boldsymbol{P_e}$ (Pa)	101352.9

$$C_F = \sqrt{\frac{2\gamma^2}{\gamma-1}\left(\frac{2}{\gamma+1}\right)^{\frac{\gamma+1}{\gamma-1}}\left[1-\left(\frac{p_2}{p_1}\right)^{\frac{\gamma-1}{\gamma}}\right]} + \frac{p_e - p_a}{p_c}\left(\frac{A_e}{A^*}\right) =$$

$$\sqrt{\frac{2(1.14)^2}{1.14-1}\left(\frac{2}{1.14+1}\right)^{\frac{1.14+1}{1.14-1}}\left[1-\left(\frac{101352.9}{172369}\right)^{\frac{1.14-1}{1.14}}\right]} + 0 = 1.6338$$

$$I_{sp} = \frac{C_F c^*}{g_0} = \frac{(1.6338)(1796.4)}{9.81} = 299.2\ seconds$$

Appendix F: Regression Rate Sample Calculations

Parameter	Value
Initial Mass, m_i (g)	356.15
Final Mass, m_f (g)	354.1
Burn Time, t_b (s)	10.019
Port Length, L (cm)	4.96824
Density, ρ (g/cm^3)	0.93
Initial Port Radius, r_i (cm)	0.5626
Oxidizer Mass Flow, $\dot{m}_{ox}$ (g/s)	0.233

$$\Delta V = \frac{m_i - m_f}{\rho} = \frac{356.15 - 354.1}{0.93} = 2.204\ cm^3$$

$$r_f = \sqrt{\frac{\Delta V}{L\pi} + (r_i^2)} = \sqrt{\frac{2.204}{4.96824\pi} + (0.6261)^2} = 0.6766$$

$$\bar{r} = \frac{r_f - r_i}{t_b} = \frac{0.6766 - 0.5626}{10.019} = 0.0113\ cm/s$$

$$G_{ox} = \frac{4\dot{m}_{ox}}{\pi\left(r_i + r_f\right)^2} = \frac{4(0.233)}{\pi(0.5626 + 0.6766)^2} = 0.19\frac{g}{cm^2 \cdot s}$$

Appendix G: Uncertainty Sample Calculations

Parameter	Value
$\dot{r}_1$, cm/s	0.01655
$\dot{r}_2$, cm/s	0.01366
$\dot{r}_3$, cm/s	0.01649
n	3
$t_{\alpha/2}$	4.303

$$\bar{\dot{r}} = \frac{\sum_i \dot{r}_i}{n} = \frac{0.01655 + 0.01366 + 0.01649}{3} = 0.01557$$

$$\sigma = \frac{\sum(\dot{r}_i - \bar{\dot{r}})^2}{\sqrt{n}} = \frac{(0.01655 - 0.01557)^2 + (0.01366 - 0.01557)^2 + (0.01649 - 0.01557)^2}{\sqrt{3}}$$

$$\sigma = 0.00165$$

$$R = t_{\alpha/2}\left(\frac{\sigma}{\sqrt{n}}\right) = (4.303)\left(\frac{0.00165}{\sqrt{3}}\right) = \pm 0.0041\ cm/s$$

Vita

Shyamal Patel was born in Riverdale, GA on April 28, 1992 to Janak and Nayana Patel. He was raised in Jeffersonville, Oh for most of his life. He attended Miami Trace High School and graduated in May 2010. He then attended the University of Michigan where he received his Bachelors' of Science in Aerospace Engineering in May 2014. Shyamal began his studies and work at the University of Texas at El Paso in January 2015. During his time at UTEP, Shyamal interned at the NASA Glenn Research Center and was selected for the Propulsion Academy at the NASA Marshall Space Flight Center.

Contact Information: spatel6@miners.utep.edu

This thesis was typed by Shyamal Patel.